# Dynamics of filaments during the edge-localized mode crash on NSTX

M. Lampert,[1, a)] A. Diallo,[1] J. R. Myra,[2] and S. J. Zweben[1]
[1)]*Princeton Plasma Physics Laboratory,*
*Princeton 08540, NJ, USA*
[2)]*Lodestar Research Corporation,*
*Boulder 80301, CO, USA*

(Dated: 21 January 2021)

Edge localized modes (ELMs) are routinely observed in H-mode plasma regimes of the National Spherical Torus Experiment (NSTX). Due to the explosive nature of the instability, only diagnostics with high temporal and spatial resolution could provide a detailed insight into the dynamics associated with the ELMs. Gas-puff imaging (GPI) at NSTX provides 2D measurements of the magnetic field aligned fluctuations (e.g. ELM filaments) in the scrape-off layer and the at the plasma edge with 2.5 $\mu$s temporal and 10 mm optical resolution. A novel analysis technique was developed to estimate the frame-by-frame velocities and the spatial parameters of the dominant structures associated with the ELMs. The analysis was applied to single ELM events to characterize the ELM crash dynamics, and then extended to a database of 159 ELM events. Statistical analysis was performed in order to find the characterizing dynamics of the ELM crash. The results show that on average an ELM crash consists of a filament with a circular cross-section which is propelled outwards with a characterizing peak radial velocity of $\sim$ 3.3 km/s. The radial velocity was found to be linearly dependent on the distance of the filament from the separatrix, which has never been seen before. The ELM filament is characterized by propagation in the ion-diamagnetic direction poloidally with a peak velocity of 11.4 km/s. The ELM crash lasts for approximately 100 $\mu$s until the radial propulsion settles back to the pre-ELM level. The experimental findings were compared with analytical theory. Two possible mechanisms were identified for explaining the observations: the curvature interchange model and the current-filament interaction model.

## I. INTRODUCTION

High confinement mode (H-mode) plasma regimes are considered to be the baseline scenarios for a future fusion power plant[1]. It was found that by applying heating power to the plasma over a certain threshold, the plasma develops a transport barrier at the very edge. This gives rise to a steep pressure gradient at the edge and in a picturesque view the original L-mode pressure profile is put onto a pedestal.

Steep gradients in any physical systems provide a source of free energy which is usually released in the form of instabilities. In the case of the edge pedestal the associated instabilities are called edge localized modes, ELMs[2]. They are quasi-periodic instabilities which could eject large number of particles and high enough energy from the plasma to be able to permanently damage the plasma facing components[3]. Predictions for ITER show that the currently available materials cannot withstand such high heat loads associated with ELMs[4], thus, the understanding of their underlying physics and the development of possible mitigation techniques are of great importance.

According to the current understanding of the ELM triggering mechanism, ideal MHD modes are driven linearly unstable by the edge pressure gradients and the edge current profiles[5,6]. The unstable modes are called peeling - ballooning modes due to the source of the instability, i.e. current and pressure, respectively. Experiments and theoretical findings agree that the peeling-ballooning instability is the driving force behind the triggering of the ELM. The results regarding the triggering mechanisms were reviewed by Kirk et al[7]. An extensive review of the ELM phenomenon was given by Zohm[8], and more recently by Leonard et al[2]

Even though the peeling-ballooning theory mechanism explains most of the ELM triggering observations, the ELM crash itself is not well understood. During the crash, filamentary structures emerge. This phenomenon were first observed experimentally on NSTX by Nishino et al[9]. The first detailed characterization of these structures was done on MAST by Kirk et al[10]. According to their observations, a filament-like structure is a structure which extends along a field line in a way that at any toroidal angle it appears to be poloidally localized and at any poloidal angle it appears to be toroidally localized. Their investigation was based on measurements performed on the MAST tokamak using Langmuir probes and high-speed video images. These findings confirmed for the first time, that the ELM crash is a filament-like structure extended along the magnetic field lines. They are generated on a 100 $\mu$s time scale, and they erupt solely on the outboard side. The occurrence of such structures confirmed the predictions of the non-linear ballooning theory[11].

Similar structures were also observed on ASDEX as measured with a dedicated $D_\alpha$ fluctuation diagnostic and on JET with Langmuir-probes[12]. These results show that the ELM filaments are propelled outwards by the $E \times B$ velocity due to polarization in the filament. The filaments could travel radially at least 10 cm (restricted by the location of the probe tip). Radial acceleration of the structures was also found on ASDEX[13] as measured with Langmuir-probes. Later observations confirmed the presence of ELM filaments on Alcator C-Mod[14] as measured with a gas-puff imaging (GPI) optical array, on JT-60[15] with Langmuir-probes, on NSTX[16,17] with a 2D GPI and on KSTAR[18] with Electron Cyclotron Emission imaging, as well. ELM filaments were also measured at COMPASS with a combination of ball-pen probe and Langmuir-probes[19].

---

[a)] Electronic mail: mlampert@pppl.gov

The observations consistently reported field aligned ELM filaments with an elevated radial velocity at the time of the crash.

The theoretical understanding of the ELM crash has evolved throughout the years of research. The most recent summary (to the best of our knowledge) of the theory behind the filamentary eruptions was summarized by Ham et al[20]. According to the summarized results, the precise mechanism behind the energy transfer from the filament to the open field lines of the SOL is unclear. Understanding the energy transfer is important to be able to mitigate damage to the device due to the associated heat and particle deposition during ELM crashes. It is believed that the dynamics of the associated filaments are directly connected with the energy transfer, thus, their characterization is of interest.

The motivation of this paper is to unfold the dynamics of the ELM filaments on a microsecond time-scale. High time-resolution characterization of the ELM filaments could reveal so far hidden features of the filament propagation and structural evolution. The investigation could also provide a basis for theoretical analysis which could lead to establishment of a new physics model for the filament formation and propagation. As explained in Section II, gas-puff imaging on NSTX allows measurement of the poloidal cross-section of the ELM filaments with high temporal and spatial resolution.

The rest of the paper is organized as follows. Section II describes the experimental setup of the GPI and the generation of the ELM database. Section III details the two-dimensional spatial displacement and the structure finding method. Section IV presents the results from a single shot calculation and also results on the characterizing structural dynamics of the ELM filaments calculated from the generated ELM database. Section V provides a discussion of the results, and Sec. VI summarizes them.

## II. EXPERIMENTAL SETUP AND THE ELM DATABASE

The results presented in this paper are focused on analysis of gas-puff imaging (GPI) measurement data on the NSTX tokamak. Hence, a brief description is given about the measurement technique and the observation geometry on NSTX. A detailed, thorough description of the diagnostic technique and measurement geometry have been reviewed by Zweben et al[21].

### A. Gas-puff imaging (GPI)

The gas puff-imaging (GPI) diagnostic measures the local fluctuations by injecting a puff of neutral gas (e.g. Deuterium or Helium) into the SOL and edge plasma and by measuring the increased line emission of the neutral - plasma collisional atomic processes.

The measured signal is a non-linear function of the local electron density and temperature fluctuations and the background neutral density. This function cannot be determined from the measurement itself, however, the shape and motion of the structures visible in the measured signal are independent of this non-linearity[22]. Thus, the velocities and shapes of the structures can be analyzed by using the GPI data without the information of the absolute electron density or temperature or their fluctuations.

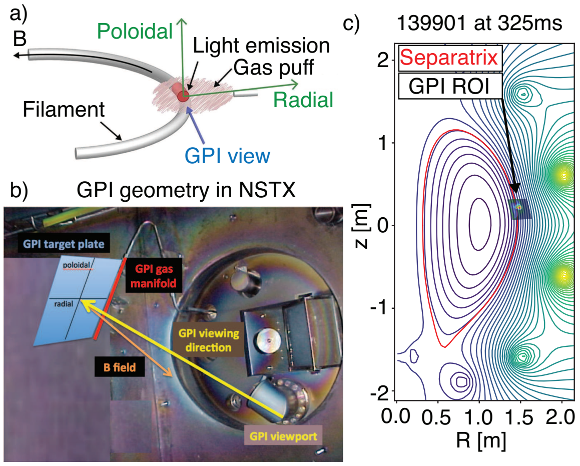

FIG. 1. a) Schematic view of the GPI measurement geometry along with the local radial and poloidal (i.e. binormal) directions (Reproduced from Zweben et al, Rev. Sci. Instrum. 88, 041101 (2017), with the permission of AIP Publishing)[21];
b) An in-vessel photo of the GPI system on NSTX along with the line-of-sight, an example magnetic field direction and the plane of measurement. Target plate used for spatial calibration is shown. (Reproduced from Zweben et al, Phys. Plasmas 24, 102509 (2017), with the permission of AIP Publishing)[23]
c) The poloidal cross-section of the GPI measurement region of interest (ROI) on NSTX along with the magnetic field reconstruction (shot 139901 at 32 5ms) and the separatrix (red).

A schematic diagram of the measurement technique can be seen in Figure 1 (a) along with the local radial and poloidal (i.e. bi-normal) directions. Ideally the following conditions need to be fulfilled for optimal spatial resolution: 2D sheet-gas injection perpendicular to the line of sight and magnetic field aligned line of sight. These conditions need to be fulfilled as much as possible to achieve optimal measurement of field aligned filamentary structures e.g. blobs or ELM filaments.

Conventional fast camera measurement techniques allow GPI to provide observation of the local fluctuation on the time scales of $\sim 1\ \mu$s to 1 ms (depending on the utilized fast camera). The effective spatial resolution is a function of the gas-puff geometry, the observation geometry and the resolution of the optics. The measurable scales could extend in principle from the ion gyro-radius ($\rho_{\mathrm{i}} \sim 0.1 - 1$ mm) to the radial size of the edge and SOL region ($\sim 10$ cm).

### B. GPI on NSTX

Results in this paper are solely from the spherical tokamak called NSTX (National Spherical Torus Experiment)[24]. NSTX is a medium-sized, low-aspect ratio spherical tokamak with a major radius of $\mathrm{R} = 0.85$ m, minor radius of $\mathrm{a} = 0.67$ m

($R/a \geq 1.26$). Its highest toroidal field can be $B_T = 0.6$ T. The most significant heating methods are the NBI (Neutral Beam Injection) with 5 MW and radio frequency heating with 6 MW.

The GPI system on NSTX has also been described in earlier papers[22,23], thus, here only a short description is given.

The measurement geometry on NSTX can be seen in Figure 1 (b). In the lower right corner, one can see the re-entrant view-port with the GPI viewing direction in yellow. The line of sight is close to parallel with the magnetic field shown in orange. However, depending on the magnetic field configuration, this angle can be slightly different. The sheet-gas is realized with a gas manifold shown in the upper left corner in red. The gas manifold has 29 gas nozzles spaced 1 cm equidistantly. The target plate used for spatial calibration is shown in light blue along with the radial and poloidal directions. Figure 1 (c) depicts an example measurement geometry in the radial-vertical plane along with the magnetic iso-flux surfaces (from EFIT reconstruction) and the separatrix. As one can see, the NSTX GPI system measures the SOL and the very edge of the plasma slightly above the mid-plane. During the 2010 NSTX measurement campaign, the time resolution of the GPI was 2.5 $\mu$s (400kHz sampling rate). The pixel resolution was $64 \times 80$ (horizontal $\times$ vertical) which provided 3.75 mm $\times$ 3.75 mm resolution (radial $\times$ poloidal) for each pixel on the target plane. The effective optical resolution was approximately 10 mm radially and poloidally, as well. During GPI measurements in 2010 the injected gas was Deuterium, $D_2$.

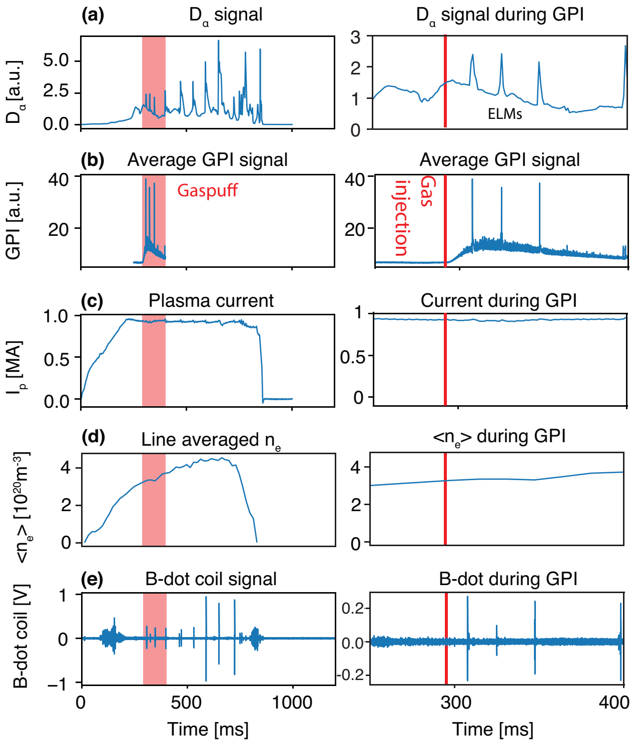

FIG. 2. Relevant plasma parameters of a GPI measurement with ELMs (shot 139901). The red area on the left depicts the time range of the gas-puff. The red line on the right depicts the time of the gas injection. Left column: the entire plasma discharge; right column: time range of the GPI measurement. a) $D_\alpha$ trace; b) GPI signal averaged for each pixel; c) Plasma current; d) Line averaged density calculated from the Thomson electron density profile measurement; e) Magnetic fluctuation measured by a B-dot coil.

### C. GPI measurement of ELMs on NSTX

Several publications have already reported on the precursor and the post-cursor oscillations of ELMs measured by GPI[16,17,25]. However, the early phases of the ELM crash were not investigated on NSTX with the means of GPI. Furthermore, the presented data analysis methods provide the highest possible temporal resolution to investigate the dynamics of the ELM crash, which have never been utilized before on the NSTX GPI data. GPI provides sufficiently high optical ($\approx$ 10 mm) and temporal resolution (2.5 $\mu$s) at NSTX for characterizing ELMs on the microsecond time scale and on the 10 mm spatial scale.

After preliminary analysis of ELM events, a single shot, #139901, was chosen with multiple ELMs in order to develop the analysis algorithms, and to gain a deeper understanding into the phenomenon from the perspective of the GPI diagnostic. The temporal evolution of its plasma parameters can be seen in Figure 2. The plots on the left depict the entire plasma discharge, with the red area showing the time interval when GPI measurement was available. On the right one can see the measurements zoomed in during the time range when GPI was available.

Figure 2 (a) shows the $D_\alpha$ radiation from Bay-C. One can see from the time trace, that the L-H transition occurred just before the GPI measurement. The first three ELMs were measured by the GPI and occurred at 307.5 ms, at 325 ms and at 345.5 ms. From these three ELMs, the analysis of the one at 325 ms is shown in detail in Section IV A. Fig. 2 (b) depicts the time trace of the GPI signal averaged over the entire image of measurement. This signal is dominated by the $D_\alpha$ emission from the Deuterium gas-puff. As one can see, the peak gas emissions around the ELMs match between the $D_\alpha$ signal and the frame-averaged GPI signal within the time resolution of the 1 kHz sampled $D_\alpha$. There was no fast $D_\alpha$ measurement available for this particular shot to compare the two types of measurement in more detail. Fig. 2 (c) depicts the plasma current during the shot, which was close to stationary in the time range of the GPI measurement. Fig. 2 (d) depicts the line averaged electron density during the plasma discharge. This signal is derived from the Thomson electron density profile measurement line averaged through its entire radial range[26]. It shows that during the GPI measurement the line averaged electron density was slowly increasing from around $3 \cdot 10^{20}$ m$^{-3}$ to $4 \cdot 10^{20}$ m$^{-3}$. Figure 2 (e) shows the signal of the B-dot coil located at $\theta = 14.15°$ above the mid-plane (Mirnov HF5). The signal was band-pass filtered to the frequency range of $[100\ \text{kHz}, 500\ \text{kHz}]$ in order to remove the low frequency oscillations and the high frequency noise from the signal. One can see that each ELM causes a small perturbation in the magnetic field measured by the coil.

The ELM event captured by the GPI system during shot 139901 at 325 ms is a typical example of what one can see during these phenomena in the GPI videos. Fig. 3 depicts 30 consecutive frames, overall a 75 $\mu$s long GPI time trace around the ELM crash.

The ELM crash time was determined to be 324.956 ms based on the GPI data (see in Sec. IV A). Before the ELM event, one can see relatively quiet activity, no coherent precursor is present. A filament-like structure enters the frame of measurement at 324.946 ms propagating in the ion diamagnetic direction, i.e. downwards. During its downwards motion, it is propelled outwards into the SOL. The radial velocity reaches its peak at $t_{ELM} = 324.956$ ms. At this frame the red title highlights the estimated time of the ELM crash based on the largest change in between the two frames (see Sec. III A). The filament reaches its highest peak intensity at $t_{ELM} + 2.5$ $\mu$s then propagates further downwards while seemingly interacting with another filament in the edge plasma. This behavior is seen in frames between $t_{ELM} + 5$ $\mu$s and $t_{ELM} + 15$ $\mu$s. The filament then exits the frame of the measurement, followed by further less intense filaments.

By observing multiple GPI measurements of ELM events one can see the following similar behavior in each event: after a quiet period or precursor activity, an intense filament-like structure is formed in the edge plasma which then crashes outwards radially, and propelled downwards poloidally in the ion-diamagnetic direction. The intensity of the ELM filament is significantly higher than any other activity e.g. edge turbulence or blobs. The spatial size of the injected filaments is comparable to other filamentary activity preceding the ELM (e.g. blobs).

### D. Generation of the ELM database

After preliminary analysis of a few ELM events (e.g. the ones in the previous section), a database was generated from H-mode shots from the 2010 NSTX measurement campaign. Based on the GPI frame-averaged signal, the ELM events were identified for each plasma discharge. The slower (1kHz) divertor Deuterium-alpha signals were also cross-checked for ELM peaks. The GPI movie of each identified event was checked for signal quality and the ones with high noise level were removed from the database. Following these steps, 159 ELM events were identified in 77 shots in which the 2010 NSTX campaign. The different types of ELMs (type I, type III and type V[27]) were not separated in the database. Upon preliminary inspection of the movie of each ELM crash, similar ELM filamentary dynamics were found in the different plasma regimes in the generated database. The goal of this research was to find the common features of the ELM crashes and the related ELM filaments not dependent on the ELM type. The database of the ELMs can be found under reference 28. The range of relevant plasma parameters for the discharges in the database are shown in Table I.

| Parameter | Range |
|---|---|
| $B_T$ | $0.35 - 0.55T$ |
| $I_p$ | $0.6 - 1.2MA$ |
| $< n_e >$ | $1.3 \cdot 10^{20} - 6.2 \cdot 10^{20} m^{-3}$ |
| $P_{aux}$ | $0 - 6MW$ |

TABLE I. Plasma parameter ranges for the discharges in the ELM database: toroidal magnetic field ($B_T$), plasma current ($I_p$), line averaged electron density ($< n_e >$), total auxiliary heating power ($P_{sum}$).

## III. DATA ANALYSIS METHODS

This section describes the steps performed during the data analysis to estimate the radial and poloidal velocities and structure sizes of the ELM filament on a frame-by-frame, 2.5$\mu$s time resolution. The first subsection summarizes the steps performed for the velocity estimation, while the second one presents the structure identification and characterization method. The fine details of the analysis methods are shown in the Appendix. The data generated during the data analysis can be found under Ref. 29.

### A. Frame-by-frame velocity estimation

In order to get the highest possible time resolution for characterization of the velocities of the exposive ELM event, a novel GPI data analysis method had to be developed. The method estimates the spatial cross-correlation function between consecutive frames, of which maximum's displacement gives an estimate of the displacement of the governing structures propagating between the two frames. The following paragraphs describe the necessary steps in order to successfully utilize this method to arrive at the frame-by-frame velocity estimation.

The first step in the method is normalization of the neutral gas response. This step is necessary because the presented cross-correlation based method is biased towards the propagation of the most intense structure. Without this step, the presence of the stationary gas response would introduce underestimation in the calculation. The normalization was done by calculating a 1 kHz Elliptic IIR (infinite impulse response) temporally filtered signal from the raw sequence of frames. Then the raw sequence of frames was divided by the filtered one frame-by-frame. The result of an example normalization step can be seen in Fig. 4 with a raw (a), a filtered (b) and a normalized frame (c). A more detailed description of this step can be found in the Appendix at A1.

The second step of the velocity estimation involves two-dimensional spatial trend subtraction (for details see Sec. A2). A cross-correlation based method needs a signal which has zero intensity offset. Ideally, all lower polynomial order (up to about fourth order) offsets need to be subtracted from the signal. This step utilizes a 2D $n^{th}$ order polynomial least squares fitting method to fit each frame in the GPI signal. This calculated trend was then subtracted from the normalized frames. Fig. 5 depicts the process of the 2D polynomial trend subtraction for an example normalized GPI frame during the ELM

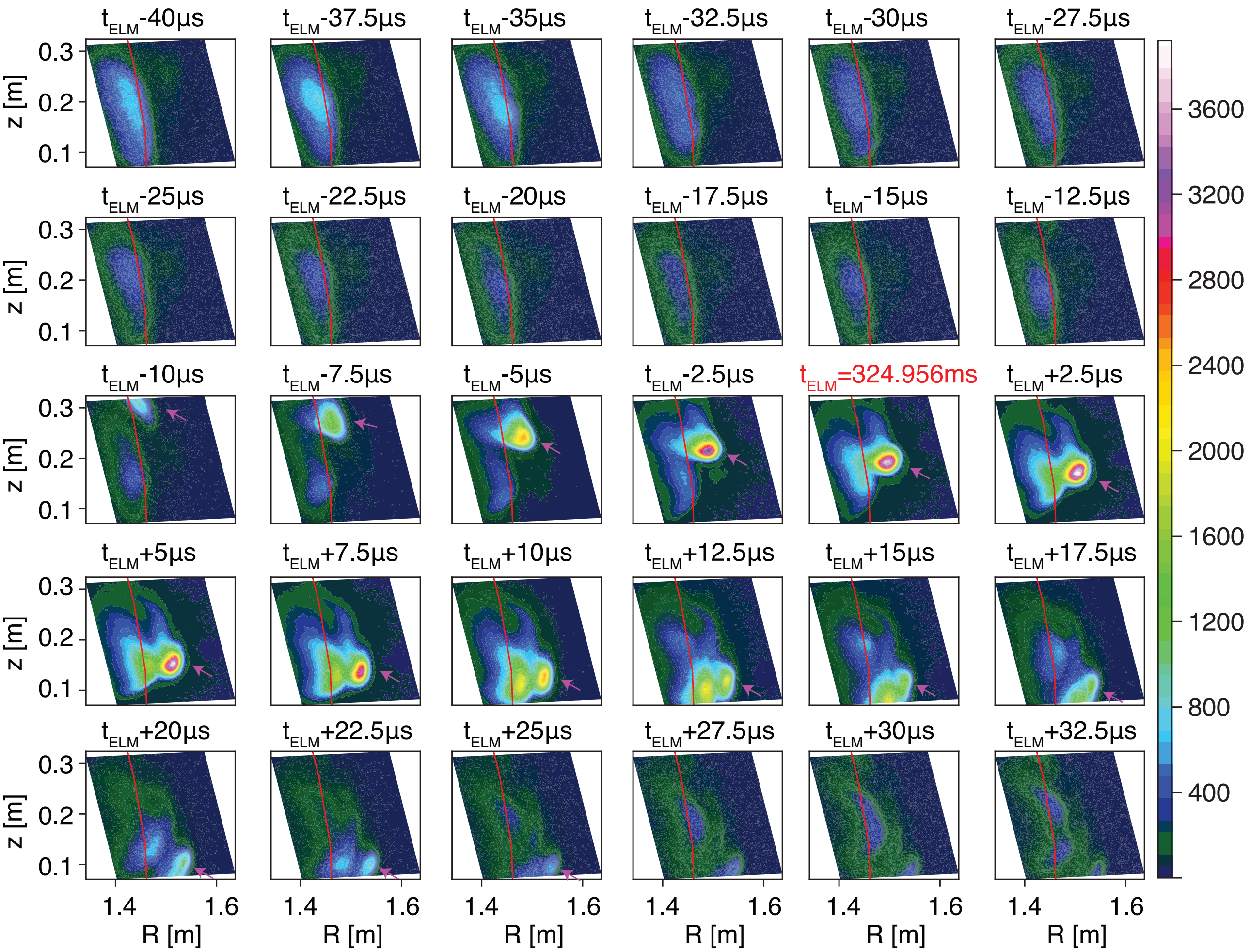

FIG. 3. The GPI measurement of an ELM event in shot 139901. A 75 $\mu$s long (30 raw frame) time series is depicted with the ELM approximately in the middle in the radial-vertical plane (projection of the target plane shown in 1). Relatively little precursor activity is seen preceding the ELM. The crash occurs at 324.956 ms (determined from the frame similarity, see at Sec. III A). An intense filament is propelled outwards radially and propagating downwards in the ion-diamagnetic direction. The separatrix is depicted with a red curve in each frame. The magenta arrow is pointing towards the ELM filament in each frame where it is present.

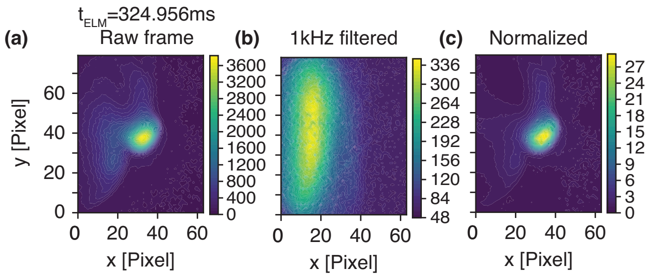

FIG. 4. Raw unfiltered frames (first row), frames from the 1kHz low-pass filtered GPI signal (second row) and normalized frames (third row) from shot 139901. Column (a) is 0.5 ms before the ELM at 324.5 ms, column (b) is at the ELM of 324.956 ms, and column (c) is 0.5 ms after the ELM at 325.5 ms.

crash along with the original normalized frame (a), the fitted fourth order 2D polynomial (b) and the subtracted frame (c).

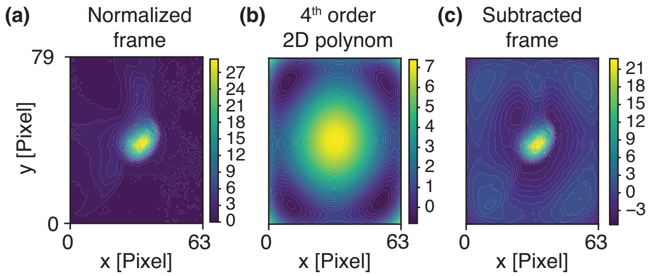

FIG. 5. a) Normalized GPI frame of shot 139901 at 324.956 ms; b) Fitted two-dimensional fourth order polynomial spatial trend; c) GPI frame after the 2D spatial trend subtraction.

The third step of the calculation estimates the 2D spatial cross-correlation function (2D CCF) between each consecutive frames (see Sec. A3). The maximum of the resulting 2D CCF is displaced from the center with the same number of

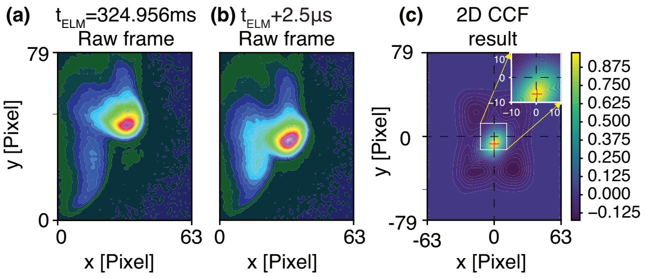

FIG. 6. a) Raw frame of 139901 at 324.959 ms; b) The next raw frame; c) The 2D cross-correlation function between the normalized, trend subtracted frame of a) and b) with the red cross showing the displacement of $[0.26\,\text{pix}, -6.72\,\text{pix}]$. The upper right corner depicts a zoomed part of the 2D CCF which makes the x, y pixel displacement more visible. Displacement in the x and y direction implies propagation radially and poloidally, respectively.

pixels in the corresponding radial and poloidal directions as the governing structure is displaced between the consecutive frames.

In the last step, the maximum of the 2D CCF was found by fitting a second order 2D polynomial onto the ±5 pixel area around the peak. The position of the maximum was then analytically calculated resulting in the pixel displacement between frame (a) and frame (b). This enhanced the pixel resolution by applying fitting of multiple pixels. The radial and poloidal displacements were then calculated from the corresponding spatial calibration coefficients and the estimated pixel displacements. Figure 6 shows an example calculation of the 2D CCF estimation with two consecutive frames around the ELM crash.

In some cases the 2D CCF velocity estimation method would have resulted in an unrealistically high velocity (e.g. a structure has just left the frame when another similar one enters). In order to mitigate this caveat a minimum acceptable level of the peak frame-to-frame cross-correlation was defined ($\rho_{\mathrm{max,thres}}$), below which the above velocity calculation was considered to be invalid. Based on thorough testing, this correlation threshold was set to $\rho_{\mathrm{max,thres}} = 0.6$ for the calculations shown in Section IV.

In order to define a unique ELM crash time for the analysis, the frame similarity coefficient is introduced. This measure equals +1 if two consecutive frames are completely the same, and -1 if they are each other's inverts. The zero lag 2D spatial correlation coefficient can be used for this purpose: $\rho_{\mathrm{FS,t_k}} = \mathrm{CCF}(\kappa_{\mathrm{x}} = 0, \kappa_{\mathrm{y}} = 0, \mathrm{t} = \mathrm{t_k})$, where $\rho_{\mathrm{FS,t_k}}$ is the frame similarity coefficient for the frame time $t_k$. This coefficient is evaluated for all consecutive frame pairs. The largest change between two frames occurs when an ELM happens, thus the minimum of the frame similarity can be used for defining the ELM crash time.

### B. Structure size estimation

Estimating the spatial size and shape evolution of individual filaments during the ELM crash could reveal important aspects of the structural dynamics e.g. filaments coalescing into a single structure. The analysis could also provide a basis for theoretical models where the current or the mass of the filament could be estimated from the current density, the electron and ion density and the size of the filament.

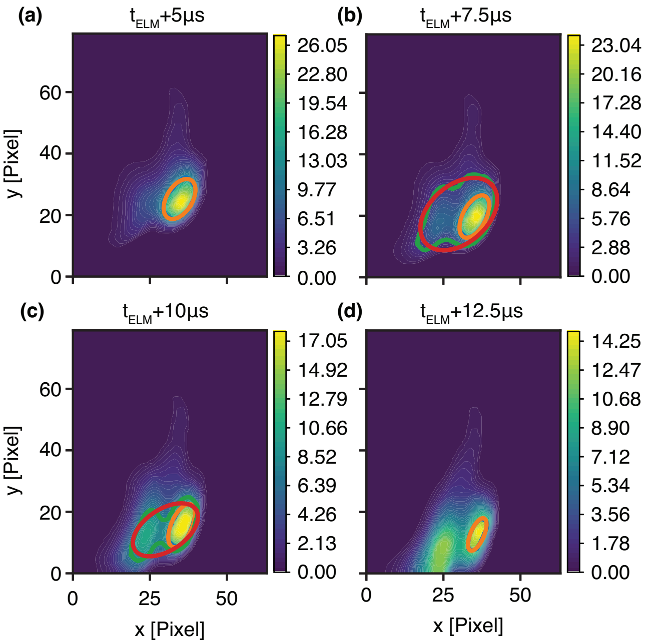

FIG. 7. Example structures found during an ELM crash in shot 139901 starting at 324.959 ms a) One structure is found (the orange ellipse fit of the green path is concealed by the fit); b) Two structures are found, the former orange and a new large structure (purple path and its red ellipse fit); c) The same two structures are found as in b), and the formation of the second one is more pronounced; d) Only one structure is found, since the second one does not contain enough enclosed paths and is about to leave the measurement area.

In the first step, the structures in each frame are identified. First, the data is pre-processed by normalizing each frame with the method presented in the previous section. Then a 5 pixel wide median filter is applied to remove excess noise. Then the frames are plot with a contour plotting algorithm which orders the contour levels by intensity and returns their coordinates one by one[30]. The plotting library also provides a method to find contour paths which are embedded into each other. Based on thorough testing, each frame was plot with 51 contour levels and a structure was identified if 5 contour paths (roughly 10% of the contour levels) with increasing levels encircled each other. (The detailed steps of the algorithm can be found in Sec. A4.) Example results of the structure identification method is presented in Fig. 7 along with the fit ellipses on the half intensity level paths.

The relevant structure size was defined as the poloidal and radial cross-section of the fit ellipse on the half intensity path. Each found structure was fit, however, in the presented results, only the one with the largest integrated intensity was considered. The goal was to determine the parameters of the ELM filament which was the most intense structure in the frame sequences. A dimensionless shape parameter, the elongation was defined to characterize whether the structures are poloidally or radially elongated. The elongation is calculated with the following expression: $(d_{pol} - d_{rad})/(d_{rad} + d_{pol})$. This metric equals 1 if the structure is purely poloidal, -1 if it is purely radial, and 0 if it is circular. The radial and poloidal position of the structures were estimated from the center of the fit ellipse. The distance between the filament and the separatrix can be estimated utilizing the estimated center and the coordinates of the separatrix from the magnetic field reconstruction (see Sec. V A).

The developed algorithms were tested on synthetic signals (for a worst case scenario see Sec. A5) and by manually cross-checking the automatic results and the movement of the center of the structures during the ELM crash. The algorithms were found to be providing good estimates on both velocities and structural parameters.

## IV. RESULTS

After developing and validating the analysis methods described in the previous sections, the algorithms were utilized to estimate parameters of the ELM events in the database. As a first approach, the methods were applied on shot 139901 to the second ELM event, which was shown in earlier sections. After analysis of that particular ELM event the parameters were estimated for each of the 159 ELM events in the database. The characterizing behavior of the ELM filaments was determined by analyzing the distribution functions of the estimated parameters. The results presented here are shown in the radial-poloidal plane which is approximately perpendicular to the magnetic field lines.

### A. Dynamics of a single ELM event

The 2D CCF based velocity estimation method and the structure parameter estimation method were both utilized to investigate the dynamics of a single ELM event. For this sample analysis shot 139901 was chosen and the ELM event was at 325 ms. The GPI frames of this ELM can be seen in Fig. 3. The time range analyzed was [324.5 ms, 325.5 ms], which is ±0.5 ms around the ELM crash time. The plasma parameters of this ELM event can be seen in Fig. 2.

Figure 8 (a) shows the time trace of the frame-averaged GPI signal. One can see that the ELM event shows up as a large peak in the middle of the time range. Several oscillations can be seen before the ELM, however, there is no clear coherent precursor oscillation. In Fig. 8 (b) one can see the maximum correlation of the 2D CCF calculated between consecutive frames in red. The correlation threshold is depicted with green. Results for the radial and poloidal velocity are only valid over this threshold. The blue plot shows the frame similarity between consecutive frames. One can see that the frame similarity reaches its minimum at the time of the ELM crash (depicted with magenta).

Fig. 8 (c) and 8 (d) show the radial and poloidal velocity, respectively, calculated with the 2D CCF velocity estimation method. The missing data points in the plot correspond to times, when the correlation maximum did not reach the threshold, e.g. between 324.7 ms and 324.9 ms. In this range no significant filamentary activity was found, thus, no velocity was estimated. The maximum radial velocity of the ELM filament is $v_{rad} = +3$ km/s outwards, which is followed by two slower outbursts. The radial velocity then decreases back in about 200 $\mu$s to the level seen before the ELM. This time is considered to be the length of the ELM crash, the time until the structures are propagating outwards after the ELM time. Further structures appear after this period of time, which

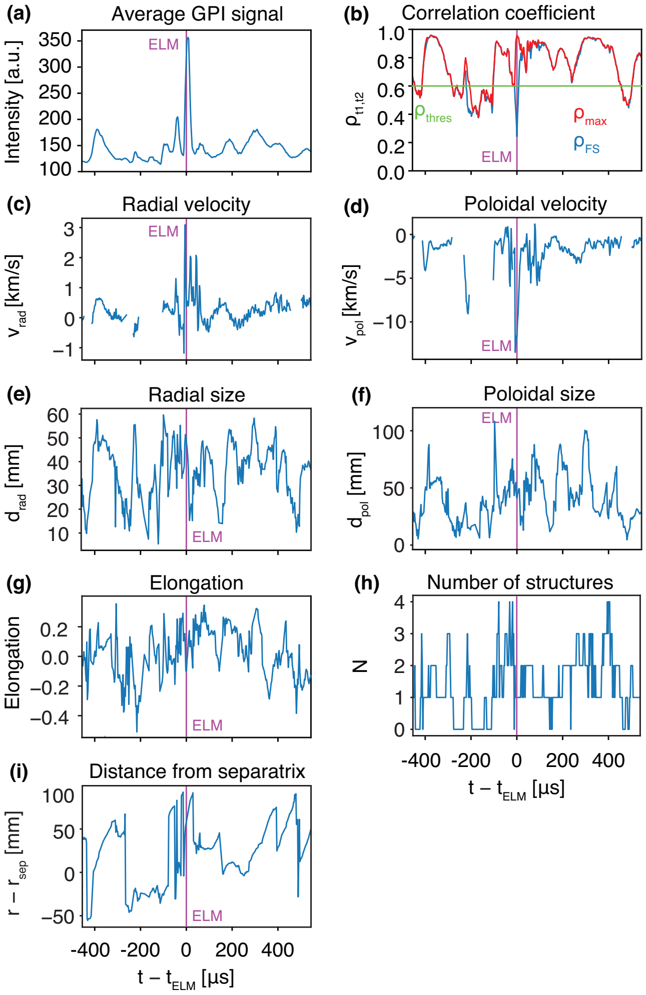

FIG. 8. Results for plasma shot 139901 for $t_{ELM} = 324.956$ ms. The timescale for all panels is shown at the bottom of each column. The missing data points in the radial and poloidal velocities are at times when the maximum correlation was under the set threshold. a) Average GPI signal vs. time with the ELM time defined by the minimum of the frame similarity (magenta); b) Maximum correlation (red) and frame similarity (blue) along with the correlation threshold (green), the ELM time is given by the minimum of the frame similarity; c) Radial velocity: d) Poloidal velocity; e) Radial size of the structure with the highest intensity; f) Poloidal size; g) Elongation; h) Number of structures; i) Distance between the center of the most intense structure in the frame and the separatrix.

could indicate post-cursor activity. The poloidal velocity has a sudden decrease right at the ELM crash time with a velocity of $v_{pol} = -13$ km/s downwards in the ion diamagnetic direction. This velocity relaxes back to around zero in 150 $\mu$s.

Figure 8 (e) and 8 (f) show the radial and poloidal sizes of the structure having the highest light intensity in each frame. These results are calculated by utilizing the structure finding and parameter estimation algorithm. The blue lines depict the size of the found structures. One can see that the radial size of the ELM filament changes between 20 mm and 50 mm, however, the size of this structure is not significantly different from the ones found in the time ranges before and after the ELM. The poloidal structure size varies between 20 mm and 80 mm. There is no significant difference between before, after and during the ELMs in the poloidal size of the occurring filaments either.

Figure 8 (g) shows the elongation, which is a function of both radial and poloidal sizes (see. III B). Positive elongation means that the structure has a larger poloidal size, while negative means larger radial size. One can see that the elongation is fluctuating with the same level before, after and during ELM times, which is consistent with the previous figures depicting the size.

Figure 8 (h) shows the number of filament structures present in the frame at a time. One can see, that just before the ELM crash time, the number of structures is higher at $N = 4$, which then decreases showing that the structures almost disappeared just before the crash where only one or two structures are present. This state is persisting until the end of the crash for about 200 $\mu$s when the structure number increases to 2-3.

During the analysis the center of the filaments was estimated from the ellipse fitting, as well. The absolute position itself is not a relevant physical parameter in the investigation of the filaments, however, the distance of the filaments from the separatrix could reveal important features of the dynamics. The coordinates of the separatrix were read from the EFIT reconstruction of the magnetic geometry of NSTX. They were interpolated linearly to match the temporal and spatial range of the GPI diagnostic. The relevant parameter was considered to be the minimum distance between the separatrix and the filament center. This quantity was then calculated for each time point of the GPI measurement. The results can be seen in Fig. 8 (i). One large outburst can be seen before the ELM crash time to about 60 mm from the separatrix in the range of $t - t_{ELM} \approx [-400\ \mu s, -200\ \mu s]$. The outburst with the largest distance occurs right before the defined ELM crash time. Another crash with similar distance from the separatrix happens 50 $\mu$s after the ELM crash. The filaments stay at 25mm outside the separatrix for approximately 200 $\mu$s after the ELM crash, after which they return nearer to the separatrix. Two filaments appear at 300 $\mu$s and 400 $\mu$s which propagate to 75 mm and 90 mm outside the separatrix.

From the results above one can see that a typical ELM crash is an explosive event seen for approximately 200 $\mu$s in the GPI measurement. The radial and poloidal velocities during the crash are significantly increased outwards and downwards (in the ion diamagnetic direction), respectively. The poloidal and radial sizes of the ELM filament were determined, however, no significant increase was found when compared to filamentary activity before and after the ELM. The structures remained elongated poloidally. The number of structures showed a tendency to decrease during the ELM crash.

### B. Characterizing dynamics of the ELM crash

Results in the previous section (Sec. IV A) showed the dynamics of the ELM crash for a single ELM event. In order to investigate the characterizing behavior of all ELM events in the database, a different approach is needed. One cannot draw conclusions for each ELM one-by-one in order to develop an understanding about the characterizing dynamics (as shown in the previous section). Preceding this, the same calculations were done for each ELM event as for the single one in Sec. IV A, but they were not analyzed manually one-by-one.

The characterizing behavior of the ELM crash was studied by analyzing the distribution functions of the estimated velocity and structure parameters. First the ELM crash times were identified based on the frame similarity (see Sec. III A). Then the distribution function of each estimated parameter was calculated in the ±500 $\mu$s time range around the ELM crash time for each parameter. The calculation was done using the valid results only, where the frame-to-frame correlation threshold exceeded 0.6. The distribution functions were calculated by dividing the value ranges of the parameters into 50 bins. Their histograms were then evaluated in the bins, and then divided by the number of valid data points. The number of structures were only divided to 10 bins since there are only whole values in this parameter, and the $90^t$h percentile was below 10.

In order to characterize the distribution functions, their median value ($50^{th}$ percentile), and their $10^{th}$ and $90^{th}$ percentile values were calculated. The median characterizes a skewed distribution better than the average, because it is not as sensitive to outliers. The $10^{th}$ and $90^{th}$ percentile values characterize the deviation of the distribution from the median and can provide an asymmetric range of deviation. The results of the calculations can be seen in Fig. 9 and Fig. 10.

#### 1. *Characterizing radial and poloidal velocities*

Figure 9 (a) and (b) depict the distribution function of the radial velocity of the filaments as a function of time for the entire ELM database and for the ELM time, respectively. The median values are shown in red, the $10^{th}$ and $90^{th}$ percentiles are shown in magenta. The median radial velocity before and after the ELM crash is approximately 300m/s. The median peak radial velocity is 3.3km/s which occurs 2.5$\mu$s (1 sampling time) before the ELM crash. The elevated radial propagation lasts for about 100$\mu$s. The $10^{th}$ and $90^{th}$ percentiles at the peak are 0.2km/s and 9.4km/s, respectively. The radial velocity decreases to 2.1km/s at $t = t_{ELM}$ and the percentiles are -1km/s and 6.3km/s (see Fig. 9 (b)).

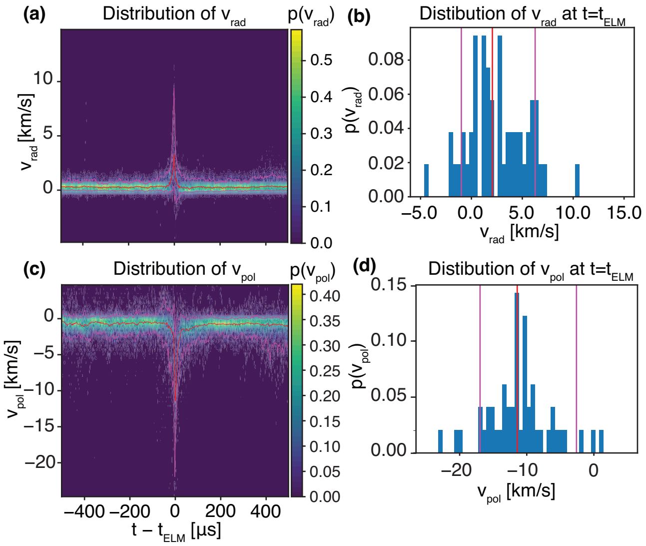

FIG. 9. Distributions of the radial and poloidal velocities vs. time for all ELM events in the database. The median of the parameters are depicted with red on the left. The 10th and 90th percentiles are depicted with magenta in each plot. (a) Distributions of the radial velocity vs. time; (b) Distribution of the radial velocity at the ELM crash; (c) Distributions of the poloidal velocities vs. time; (d) Distribution of the poloidal velocity at the ELM crash.

Figure 9 (c) depicts the distribution function of the poloidal velocity of the filaments as a function of time for the entire ELM database. As for the radial velocity, the median values are shown in red, the 10th and 90th percentiles are shown in magenta. The median poloidal velocity before and after the ELM crash is approximately -700m/s. The negative sign stands for the ion diamagnetic direction. The median poloidal velocity is -11.4km/s at the ELM crash. The 10th and 90th percentiles at the ELM crash are -2.6 km/s and -22 km/s, respectively. The distribution function of the poloidal velocity at the ELM crash is depicted in Fig. 9 (d).

It has to be noted, that the GPI observation is aligned to the typical pitch angle of NSTX plasma regimes. Deviations from the typical angle results in a projection of the actual poloidal velocity onto the target measurement plane introducing uncertainty in the velocity estimation. However, these angle deviations are small on NSTX. Furthermore, the uncertainty of the velocity estimation method is larger than the uncertainty caused by the misalignment, thus, this effect can be neglected.

### *2. Characterizing structural parameters*

The distribution functions of the spatial parameters of the ELM filaments were also investigated. The distribution functions and the corresponding percentiles were calculated for the filament size, elongation, number of structures and the distance of the structures from the separatrix. The results of the calculation can be seen in Fig. 10. On the left the time evolution of the distribution functions is shown. The median value is plotted with red, while the 10th and 90th percentiles are plotted with magenta. The plots on the right show the distribution functions of each parameter at the ELM crash.

Fig. 10 (a) and (b) show the distribution of the radial size for the analyzed time range and for $t = t_{ELM}$, respectively. The median radial size remains relatively constant before the ELM crash at a level of 30mm. This value increases to 49 mm at the ELM crash. The 10th and 90th percentiles are 31 mm and 69 mm at the ELM crash, respectively. The median radial size level is increased to 35 mm after the ELM crash.

Fig. 10 (c) and (d) show the time evolution of the distribution function of the poloidal size for the analyzed time range and for $t = t_{ELM}$, respectively. The median poloidal size is approximately 40mm before and after the ELM crash. The poloidal size at the ELM crash is 47 mm. The 10th and 90th percentiles at the ELM crash are 32 mm and 72 mm, respectively. The poloidal size shows a smaller increase than the radial size has at the ELM crash.

Fig. 10 (e) and (f) show the time evolution of the distribution function of the elongation for the analyzed time range and for $t = t_{ELM}$, respectively. The level of the median elongation undulates slightly around 0.1 before and after the ELM crash. About $35\mu$s before the ELM crash the elongation is increased to 0.21 which then rapidly decreases to 0.035 at the ELM crash. This value is close to zero, which indicates that the characterizing shape of the filament at the ELM crash is close to circular. The 10th and 90th percentiles at the ELM crash are -0.24 and 0.2, respectively. This large spread is a result of the definition of the elongation and the relatively large spread of the poloidal and radial sizes from which the elongation was calculated.

Figure 10 (g) and (h) show the time evolution of the distribution function of the number of structures identified for the entire analyzed time range and for $t = t_{ELM}$, respectively. The median structure number is 2-3 before the ELM crash. The 10th and 90th percentiles are 1 and 4-7, respectively. The median number of structures is 1 at the ELM crash with the percentiles being 0 and 2 (see Fig. 10 (h)). This reflects that the characterizing behavior of the structures at the ELM crash is coalescing, multiple structures merge into 1 or 2 structures. Right after the ELM crash the median increases to 2. The characterizing number of structures is 3 at $200 - 300\mu$s after the ELM crash. At around $350\mu$s after the ELM crash the median number of structures decrease back to the same level as it was before the ELM crash.

Figure 10 (i) and (j) depict the time evolution of the distribution function of the distance of the filaments from the separatrix for the entire analyzed time range and for $t = t_{ELM}$, respectively. One can see that the median distance is approximately +20mm before the ELM crash and the percentiles are -15 mm and +60mm. The negative sign stands for inside the separatrix, while the positive is outside. It has to be noted that the accuracy of the magnetic field reconstruction is in the range of 10mm. The outburst of the ELM filaments sets on approximately $30\mu$s before the ELM crash and it reaches a median distance of 67 mm. The 10th and 90th percentiles of the distribution at the ELM crash are 20mm and 105mm, respectively. The median distance settles back to the original level in approximately $330\mu$s after which a slight increase occurs.

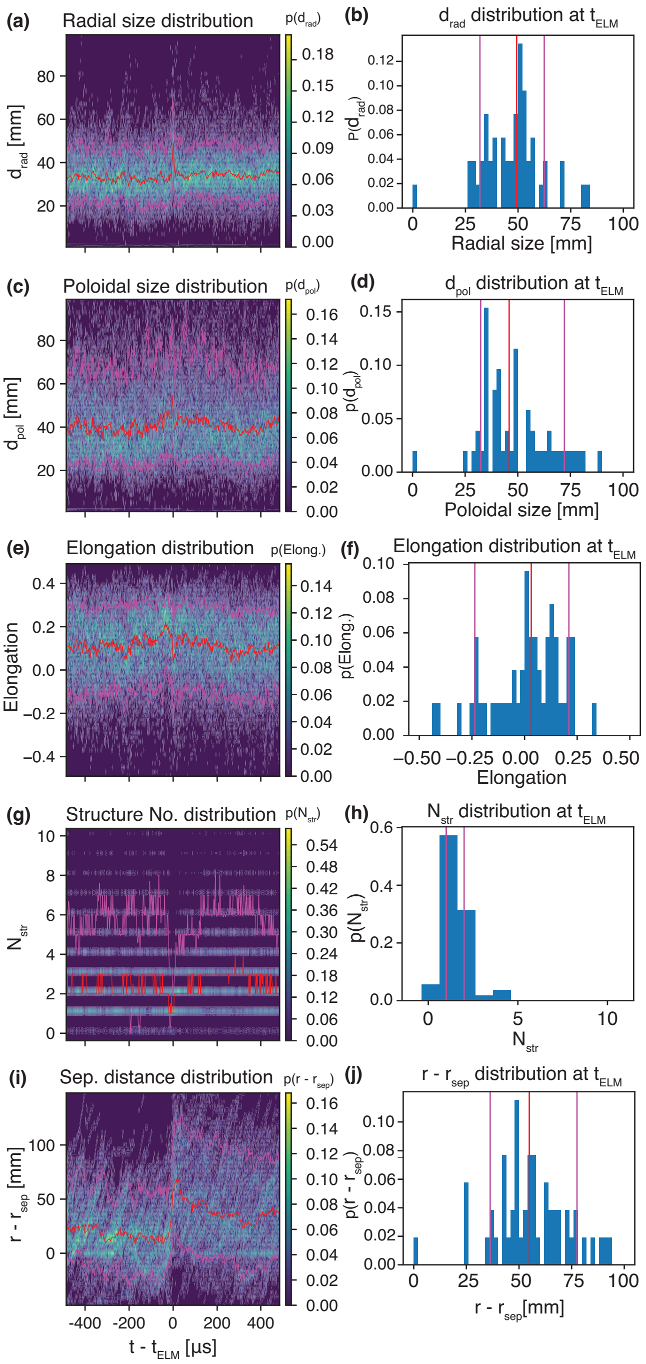

FIG. 10. Distribution of structure sizes, elongation and number of structures calculated for the entire ELM database with the structure identification method. The distribution is calculated for each time point. The median of the parameters is depicted with red on the left. The 10th and 90th percentiles are depicted with magenta in each plot on the left. The distributions at $t_{ELM}$ are shown in the right column. (a)-(b) Distribution of the radial size of the most intense structures in a frame; (c)-(d) Distribution of the poloidal size of the most intense structure in a frame; (e)-(f) Distribution of the elongation during the ELMs; (g)-(h)) Distribution of the number of structures during the ELMs. (i)-(j) Distribution of the distance between the most intense structure and the separatrix.

## V. DISCUSSION

In the first part of this section (Sec. V A), the results are discussed by analyzing their dependence on each other. In Sec. V B the dependence of the sizes and the velocities on several plasma parameters is discussed. Sec. V C connects the results to analytical theory. In Sec. V D the observed poloidal velocities are compared to the ion-diamagnetic drift velocities at the ELM crash time. The last section, Sec. V E puts the results into context of previous experimental findings.

### A. Dependence of the ELM crash parameters on each other

This section presents the dependencies of the characterizing ELM database results in Sec. IV B on each other. The conventional approach is to calculate the correlation-coefficients between each parameter (resulting in a Pearson-matrix). This approach, however, cannot provide insights into the time dependence of the results e.g. the pre-ELM, the ELM crash, and the post-ELM period. Therefore, the relevant parameters are plotted against each other. The dependence between every parameter was determined, however, in the followings only the most physically significant and relevant results are presented.

Figure 11 depicts the dependencies between the median parameters. The color bar on the right shows the timing with respect to the ELM crash. The blue lines connect data points which are consecutive in time.

Fig. 11 (a) depicts the relationship between the characterizing radial and poloidal velocity of the ELM filament. As one can see, during the ELM crash the radial velocity reaches its peak one sample time (2.5 $\mu$s) before the poloidal velocity does. There is close to linear dependence between the two velocities in the 20 $\mu$s time range both before and after the crash. The radial velocity relaxes back to approximately the same level as it was before the ELM. The poloidal velocity relaxes back to its original level in approximately 200 $\mu$s.

The dependence between the radial and poloidal sizes is depicted in Fig. 11 (b). Positive correlation can be seen between the radial and the poloidal sizes. The few outliers are caused by the ELM crash, when the structures are close to circular.

Fig. 11 (c) depicts the dependence between the median radial velocity and the distance between the center of the filament and the separatrix. As one can see before the ELM crash (blue/green patch of data points), the filaments are around the separatrix (considering the approx. 10 mm accuracy of the magnetic reconstruction and the 10 mm optical resolution of the GPI). As was also seen in Fig. 10 (i), 25 $\mu$s before the ELM crash the filament accelerates outwards radially. The radial velocity during this outwards motion is approximately linearly dependent on the distance of the filament from the separatrix. This behavior has never been seen before. The radial velocity reaches its peak at $r - r_{sep} = 49$ mm, and then it rapidly decelerates back to the orange and purple patch of data points.

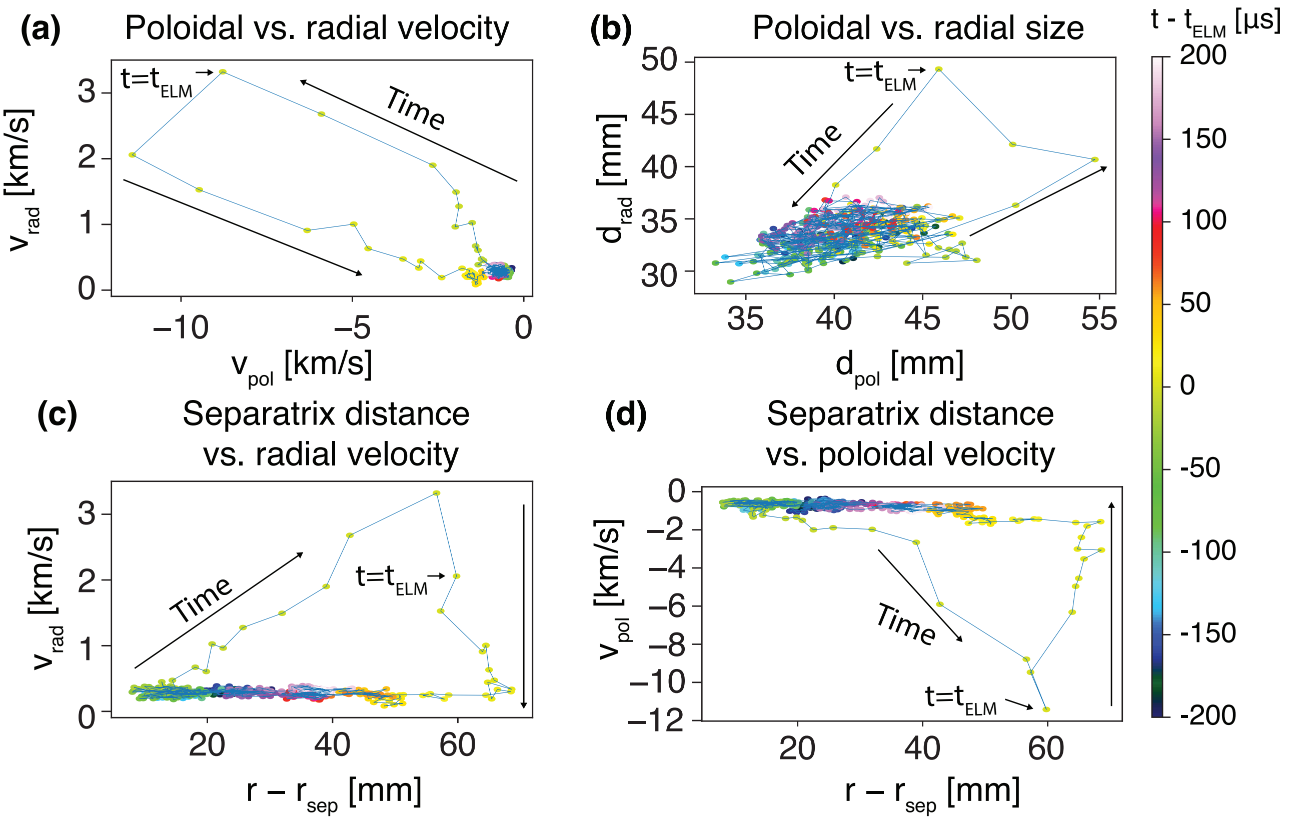

FIG. 11. Dependence of the significant parameters on each other. The time of each point is presented with a different color. The color bar on the right shows the time-color coding. The consecutive points are connected with a blue line. The estimated uncertainties are also shown. a) Connection between the poloidal and radial velocities; b) Connection between the poloidal and radial sizes; c) Connection between the distance from the separatrix and the radial velocity; d) Connection between the distance from the separatrix and the poloidal velocity.

The dependence between the poloidal velocity and the distance of the filament's center from the separatrix can be seen in Fig. 11 (d). Before the ELM crash, the poloidal velocities are between 0 and -2 km/s (the minus sign denotes the ion diamagnetic drift direction). As the filament propagates outwards, its poloidal velocity increases, however, the increase is faster than linear. The same behavior can be seen after the crash. The velocity relaxes back to approximately the original level.

## B. Dependence of the filament parameters on plasma parameters

After determining the trends between the estimated ELM filament parameters, their dependence on the edge plasma parameters were investigated. The edge plasma temperature, density and pressure profiles were fitted and the maximum gradients were determined from the profiles. The magnetic field reconstruction on NSTX provided the current density profile.

Several parameters were determined from the fitted plasma profiles such as the maximum gradient, the global gradient, and the width of the pedestal. However, non of these parameters showed significant correlation with the estimated ELM filament parameters. It is suspected, that the reason for this negative result is the relatively low temporal resolution of the Thomson-scattering diagnostic, which could only provide profiles on a 16ms time resolution. It is expected that the plasma profiles evolve on a ms time-scale between the ELMs. However, there were only 9 cases from 159 ELMs where the profiles were within 1ms compared to the ELM times.

The plasma current density profile is reconstructed during the magnetic field reconstruction on NSTX. The peeling-ballooning theory predicts the stability boundary of the plasma on the pressure-current density plane. Hence, it is expected that the edge current has influence on the ELM filament parameters. The relevant edge current density was identified as the value at the maximum density gradient, because according to the peeling-ballooning theory, the ELM is triggered at the position of the largest gradient. Fig. 12 depicts the results of the dependence calculations between the edge current density at the maximum density gradient and the ELM filament sizes and velocities at the ELM time.

Fig. 12 (a) shows the dependence between the edge current density ($j_{edge}$) and the radial size. The results have large scatter, however, a weak positive trend can be seen between the two parameters. This trend meets the expectations, and expla-

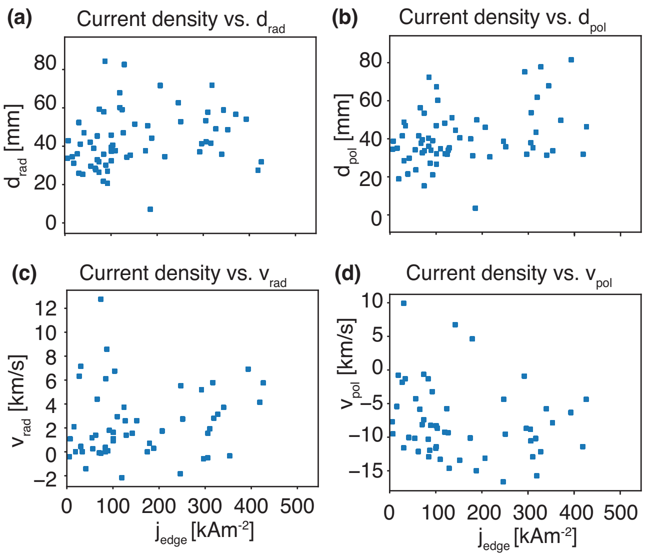

FIG. 12. Dependence of filament sizes and velocities at $t = t_{ELM}$ on the edge current density. (a) Current density vs. radial size; (b) Current density vs. poloidal size; (c) Current density vs. radial velocity; (d) Current density vs. poloidal velocity.

nation for it is given in V C. Fig. 12 (b) shows the dependence between $j_{edge}$ and the poloidal size. The same weak trend can be seen as for the radial size.

Fig. 12 (c) and (d) depict the dependence of the radial and poloidal velocities on $j_{edge}$, respectively. A weak positive trend can be seen between $v_{rad}$ and $j_{edge}$, which can be explained by the current-filament theory shown in Sec. V C 2. The poloidal velocity shows a weak negative correlation with the edge current density.

In order to provide a more accurate dependence study between the plasma parameters and the ELM filament parameters, more accurate plasma profiles (e.g. from numerical modelling) and magnetic reconstructions (e.g. from kinetic EFIT) would be needed. Performing these more accurate calculations are outside the scope of this paper, and will be considered during future research.

## C. Connection with theory

In this section a connection between the observations and analytical theory is discussed. In the first subsection the existing papers are summarized shortly. In the second subsection of the section the possible underlying mechanisms behind the radial acceleration are discussed; namely, the curvature-interchange mechanism and the current-filament interaction model.

### *1. Theoretical models for the ELM filaments*

The non-linear peeling-ballooning model, also known as the Wilson and Cowley model, explains the early nonlinear evolution of the ballooning mode and shows that the ELM is en explosive event growing faster than exponential[11]. This theory gives an explanation for the formation of the filamentary structures appearing at the ELM crash on the time scale of $50-100\ \mu$s. In our results, the time scale of the crash is between $100-200\ \mu$s. The presence of filaments in our observations can be explained by the Wilson and Cowley model.

The theory for the early non-linear phase was developed by Ham et al into a fully nonlinear MHD model which gives an explanation for the saturation of the filament displacement[31,32].

Several models were established for explaining the transport mechanisms behind the ELM filaments. In a model established by Kirk et al it is assumed that the filament remains connected to the confined plasma and to the divertor directly, causing a leak from the core[33]. In our measurements GPI only covers a small two-dimensional cross-section of the plasma while the model is describing a three-dimensional effect. Hence, it was not possible to find evidence for the filament having connection with the confined region.

Another model was established later on by Evans et al[34]. The model assumes that after the initial linear peeling-ballooning growth phase of the ELM the thermoelectric currents flowing through relatively short pedestal plasma flux tubes are amplified causing the explosive growth of the instability. These also account for connecting the inner and outer divertor target plates.

A theoretical model specific to the current-carrying aspect of ELM filaments was proposed by Myra[35]. Current conservation provides a mechanism that can propel the ELM filament outwards from the main plasma. At the time of birth of the ELM filament from an underlying peeling-ballooning mode, areas with both positive (filament) and negative (hole) current density appear. These anti-parallel currents repel each other. Whether this mechanism could account for the observed ELM acceleration is discussed in more detail below.

Further theoretical insight into the dynamics of the ELM filaments is provided by D'Ippolito et al[36]. Two electromagnetic mechanisms are reviewed. The first mechanism is the aforementioned repulsion, while the second is field line bending[37]. This effect is a three-dimensional effect and it is not directly captured by the GPI measurement.

### *2. Proposed models for explaining radial acceleration*

ELMs are believed to originate from unstable peeling-ballooning modes, and are driven by a combination of the gradients of parallel current and pressure in the presence of curvature. It is therefore reasonable to investigate whether the observed ELM acceleration can be explained by mechanisms related to curvature-interchange or current-filament interaction.

The curvature-interchange mechanism is described by an effective gravitational acceleration

$$g_\kappa = f_\kappa \frac{c_s^2}{R} \tag{1}$$

where $f_\kappa \approx (p_{max} - p_{bg})/(p_{max} + p_{bg}) \leq 1$ is a form factor that accounts for the amplitude of the filament pressure perturbation ($p_{max}$) above background ($p_{bg}$), $c_s$ is the sound speed, and R is the radius of curvature, approximately the major radius of the torus. According to standard blob theory, $g_\kappa$ drives charge polarization in a blob, and results in radial $E \times B$ convection[38]. Since Eq. 1 is only a rough analytical estimate of the curvature-interchange driving force in a real device, we also regard $f_\kappa$ as accounting for other factors arising for example from device geometry and the filament profiles along and across the magnetic field and dissipative or retarding forces.

The other model under consideration is the current-filament interaction model[35]. Similar models were also applied to explain the ELM filament dynamics on the Pegasus Toroidal Experiment[39,40]. In this model, the fundamental force is the magnetostatic force between two anti-parallel current carrying 'wires'. One 'wire' is the ELM filament which is postulated to carry away a fraction of the current density at its birth location and transport that current outward radially. The other 'wire' is the current hole left behind. In the thin wire approximation, which is only appropriate when the separation of the ELM and its current hole greatly exceed the ELM radius, the accelerating force is

$$g_J = -\frac{\mu_0 I_1 I_2}{2\pi^2 d m_i n_i \delta_b^2} = \frac{\mu_0 J_\parallel^2 \delta_b^2}{2 d m_i n_i} f_J^2 \tag{2}$$

where $I_1 \approx -I_2$ are the currents contained in the filament and the hole, d is their separation, $m_i n_i$ is the plasma mass density and $\delta_b$ is the filament radius[35]. In the second form of Eq. 2, we estimate $I_1 \sim f_J J_\parallel \pi \delta_b^2$ where $J_\parallel$ is the edge plasma current density at which the filament forms, and $f_J \approx J_b/J_\parallel < 1$ is the radio of the current density in the ELM filament ($J_b$). As discussed in relation to the curvature interchange mechanism, Eq. 6 is only a rough analytical estimate, and the form factor $f_J$ absorbs other corrections.

Equation 2 is the thin wire approximation for infinitely long filaments; it is sufficiently accurate for $d/\delta_b > 1.7$. For smaller d, it is straightforward to generalize the thin-wire model by numerical integration. For uniform disks of radius $\delta_b$ carrying anti-parallel current density, we find that $g_J$ maximizes for $d/\delta_b \sim 1.3$ at a value that is about 0.80 lower than the thin-wire estimate. For still smaller $d/d_b$ the thin wire estimate becomes increasingly inaccurate: when $d/\delta_b = 0$ the uniform disk result goes to zero, not infinity.

The momentum or vorticity equation[38] governing the motion of ELM filaments contains terms representing inertia, accelerating forces from $g_\kappa$ and $g_J$, and retarding forces from magnetic line bending. If we assume that the line bending force is subdominant, then inertia, dv/dt, balances the g forces (this is the so-called inertial regime of blob-filament theory) and it is reasonable to compare the measured acceleration of the ELMs with $g_\kappa$ and $g_J$ to assess the plausibility of these mechanisms as an explanation. Line bending could reduce the net acceleration of the ELM, but it cannot be dominant; otherwise, the peeling-ballooning mode would not be unstable in the first place.

To assess the plausibility of the two mechanisms, the factors $f_i$ (i = $\kappa$ or J) are estimated by solving for them from $a_{GPI} = g_i$ where $a_{GPI}$ is the measured radial acceleration from the ELM database (the slope of the linear fit on $v_{rad}$ for the time range of $[t_{ELM} - 10\mu s, t_{ELM}]$ for each ELM), $g_i$ are obtained from Eqs. 1, and 2 using approximate experimental data for the ELM parameters. In particular, $n_e$ and $T_e$ for the ELMs were taken from edge Thomson scattering measurements. $J_\parallel$ was taken from EFIT magnetic reconstructions from the radial position, where $\nabla n_e$ was the largest. It was assumed that the ELM filament is born in edge at the location where the density gradient is maximum. The plasma and current density parameters that are assumed to characterize the ELM in the analysis were taken at the birth location. This location could be determined with reasonable certainty, and detailed analysis of a selected discharge indicated that this location is close to where the current density gradient also maximizes. Error bars for the form factors were estimated from the scatter in the edge Thomson scattering measurements and from the estimated uncertainty in determining $\delta_b$. Error bars for the measured accelerations were estimated from the uncertainty of the slope during the linear fitting of $v_{rad}$. Results are shown in Figs. 13. In making this comparison, the uniform disk model has been employed and only points with $d/\delta_b > 1$ were retained.

Figure 13 shows the maximum total acceleration $g_\kappa + g_J$ from both mechanisms assuming $f_\kappa = f_J = 1$ plotted against the measured acceleration $a_{GPI}$. It can be seen that the maximum total available acceleration from the model easily exceeds the measured acceleration, consistent with the fact that the deducted form factors are mostly less than 1. These mechanisms are strong enough to explain the observations, even with the addition of mitigating forces. Although there is considerable scatter, there is some tendency for $g_\kappa + g_J$ to increase with $a_{GPI}$.

Several other features of the plots in Fig. 13 are worth noting. If a particular mechanism (curvature or current filament interaction) is the only active mechanism, then $f_\kappa$ or $f_J$ should always be less than one in order to be a viable explanation. This is the case in both plots for the vast majority of the data (including error bars). For example, the measured acceleration in shots with $f_\kappa \sim 1$ could be explained by the curvature mechanism assuming the ELM provides an order unity pressure perturbation.

For ELMs with $f_J \sim 1$, the measured acceleration could be explained by the current filament interaction mechanism if the ELMs carry a substantial fraction of the background parallel current $J_\parallel$ in the edge plasma at their presumed birth location. For the NSTX data, $f_J \sim 1$ would imply an ELM current of the order of a few hundred Amperes, which is not unreasonable given the measured ELM currents in other devices (See Sec. V E).

Thus, we conclude that either mechanism has sufficient strength to contribute to the acceleration of the ELM filaments. However, the current filament interaction mechanism has the theoretical possibility of qualitatively explaining some other features of the measurements, as discussed next.

It was noted in Sec. IV (see Figs. 8 and 10) that the ELM filaments tend to become nearly circular (elongation $\approx 1$) near

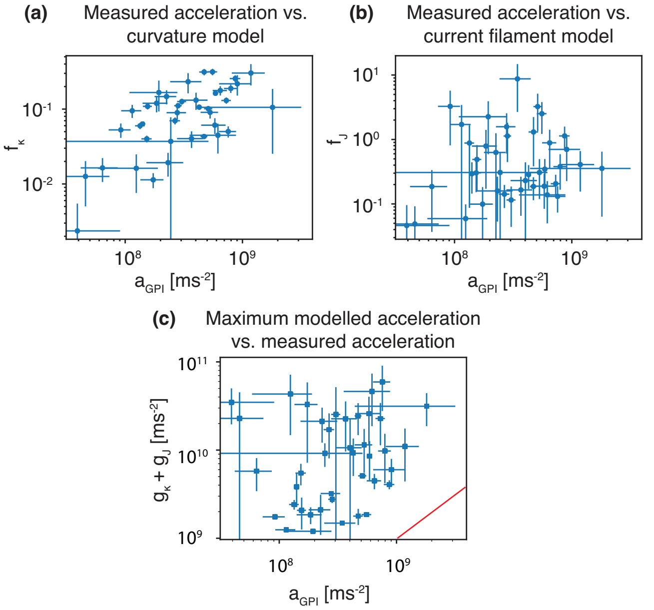

FIG. 13. (a) Comparison of the factor $f_\kappa$ from the curvature model with the measured acceleration for ELM filaments in the database; (b) the same comparison for $f_J$ from the current filament model. In both cases a factor $f_\kappa$ or $f_J$ of order unity or less indicates that the associated mechanism is of sufficient strength to give rise to the measured acceleration. (c) maximum total acceleration $g_\kappa + g_J$ from both mechanisms assuming $f_\kappa = f_J = 1$ (red line: $g_\kappa + g_J = a_{GPI}$).

the ELM crash time, and that multiple filaments (within the GPI view) also tend to coalesce at the crash time resulting in a structure number of 1. Both of these observations are qualitatively expected for current-filament interaction. For the same reason that anti-parallel currents in a filament and hole repel, parallel currents in adjacent filaments, or within an individual filament, attract. This naturally leads to coalescing and circularization.

The current filament interaction model also provides a theoretical possibility for understanding the observed poloidal acceleration. In the presence of flow shear, the ELM filament and current-hole acquire poloidal separation and the poloidal motion is then also subject to the same current-repulsion force mechanism as the radial one.

Finally, the abrupt end of the acceleration phase is prominent in Fig. 11 (c). The change from acceleration to deceleration in Fig. 11 (c) is sudden; and, in fact, the deceleration is very large and occurs at a specific radial location. This is suggestive of a discrete process. One hypothesis is that during the initial phase when the ELM filament is observed to accelerate into the SOL at the mid-plane, it remains magnetically connected to the closed surfaces at its foot-points near the top and bottom of the torus. This is made possible by magnetic line bending. But then at the crash, either one or both foot-points of the filament reconnect with field lines in the SOL at which time the heat and current drain quickly. This would bring the radial motion by both curvature and current mechanisms to a sudden stop. For the present work, this idea is theoretical and speculative as there is no available corroborating data. However, the idea of reconnection has been discussed in several ELM review articles and references therein[2,41].

Most of the preceding observations are difficult to understand based on the curvature drive mechanism alone. Possible exceptions are coalescence which can sometimes occur for curvature driven blobs and radial, but not poloidal, acceleration which could be accounted for by other mechanisms associated with propagation down a density gradient, as discussed in the blob context by Bodi et al[42].

We close this section with a qualitative observation. One of the most striking features of the present data is the rapid and nearly constant acceleration of the ELMs from the time when they first emerge to when they crash. There have been many experimental papers on blobs, but to our knowledge a qualitatively similar acceleration of blobs has never been reported in these experiments, or in fact in blob turbulence (as distinct from seeded blob) simulations. Why are ELMs and blobs different in this respect? A definitive answer is not possible from the information at hand, but theoretical considerations suggest one possible speculation.

An ELM forms from a rapidly growing MHD instability. Furthermore, as the instability grows, nonlinear effects such as its explosive character take over further shortening the time scale[43]. Thus, ELMs may be seeded almost instantaneously but require time to accelerate up to a terminal velocity consistent with the $g_J + g_\kappa$ forces. Blobs on the other hand are expected to evolve out of slower growing turbulence for which the blob velocity is already a characteristic velocity of the underlying linear mode. (See e.g. the discussion of the correspondence principle in Ref. 36.) Simulation modeling of nonlinear ELM evolution, in conjunction with a direct experimental measurement of the current in the modeled ELM filament would likely be required to test this hypothesis.

### D. Relationship between the poloidal filament velocities and the ion-diamagnetic drift velocity

The poloidal propagation of the ELM filaments is characterized by $v_{pol} = 11.4\mathrm{km/s}$ median poloidal velocity (see Fig. 9) in the ion diamagnetic drift direction. According to the peeling-ballooning theory, ELM filaments originate from inside the separatrix where their poloidal motion is determined by the local ion diamagnetic drift velocity. By calculating the ion-diamagnetic drift velocity profile, and relating the estimated poloidal velocities to them, one could calculate the birth position of the filaments. This calculation assumes that the filament's poloidal motion is not influenced by the shear layer at the separatrix or other effects like the previously discussed current-filament interaction significantly. The ion diamagnetic drift velocity can be calculated with Eq. 3.

$$v_{i,diam} = -\frac{\nabla p \times B}{q n_i B^2} \approx -\frac{|\nabla p|}{q_i n_i B} \tag{3}$$

In the calculation pure poloidal propagation is assumed perpendicular to the magnetic field. The pressure gradient profile is estimated from the radial pressure profile provided by

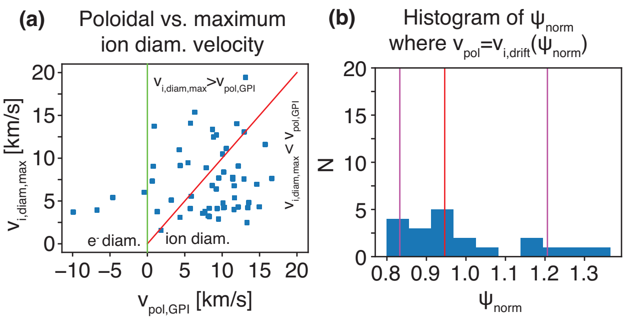

FIG. 14. (a) Poloidal velocity of filaments vs. maximum of the ion diamagnetic drift velocity profile. The red line depicts $v_{pol} = v_{i,diam}$, the green line separates the ion and electron diamagnetic direction; (b) Histogram of positions where $\mathrm{v_{pol}} = \mathrm{v_{i,diam}}$ with the median (red), and the $10^{\mathrm{th}}$ and $90^{\mathrm{th}}$ percentiles (magenta).

Thomson scattering. The ion density profile is assumed to equal the electron density profile, which is provided by the same diagnostic. The ion diamagnetic drift velocities were calculated for each ELM in the database for the closest time point to the ELM crash time.

Fig. 14 (a) shows the maximum values of each ion diamagnetic drift velocity profiles plotted against the estimated poloidal velocity at $\mathrm{t_{ELM}}$. In the majority of the cases, $v_{i,diam}$ is lower than the estimated poloidal velocity. This means that in most cases the ion diamagnetic drift cannot be the only mechanism driving the poloidal propagation. The missing portion of the driving force could originate from the current-filament mechanism described in Sec. V C 2.

In the rest of the cases, the ion-diamagnetic drift velocity could account for the observed poloidal velocity During the analysis of these cases, the normalized poloidal flux position was found, where the observed poloidal velocity equals the radial ion diamagnetic velocity profile. The range of these locations was divided to 10 bins, and the number of cases were counted in each bin. The results of this calculations are shown in Fig. 14 (b).

The median and the $10^{th}$ and $90^{th}$ percentiles are depicted with red and magenta lines, respectively. The median is $\Psi_{\mathrm{norm}} = 0.95$, and the $10^{\mathrm{th}}$ and $90^{\mathrm{th}}$ percentiles are 0.83 and 1.2, respectively. The median value itself could be physically feasible in these cases, since the 0.95 value is close to and inside the separatrix, where the filaments are theoretically originating from. However, the distribution has a large deviation from the median. Due to the small number of positive cases and the large deviation no strong statement can be said about the birthplace of the filaments. Providing more accurate estimation on the observed poloidal velocities would require numerical modelling, which is outside the scope of this work, and will be considered during future research.

## E. Comparison with previous experimental results

As presented in Sec. I, ELM filaments were investigated extensively on many different machines with different diagnostic techniques. Most of the previous results were originating from Langmuir-probe measurements. A few publications are based on measurements with fast visible imaging, Thomson-scattering and reflectometry. The following sections put the presented NSTX results into perspective with results on other machines. The comparison is solely based on the ELM filament findings in the SOL, thus, e.g. the triggering mechanism inside the separatrix is not discussed. A summary of the results discussed below for each machine can be seen in Table II.

### *1. Comparison with earlier results from NSTX*

Several papers have already been published on results from NSTX. The first observation of ELM filaments on NSTX was done by Nishino et al[9] with the use of fast visible imaging.

Maingi et al[27] characterized type V ELMs on NSTX with several diagnostics including fast visible cameras, interferometer, magnetic probes and gas puff imaging. The size and velocity of the filaments were estimated by analyzing measurements of toroidally adjacent interferometry channels. Their rotation speed was estimated to be $\sim$ 10 km/s, and their perpendicular length was in the range of $\sim$ 10cm. The filaments were found to be drifting radially outwards while rotating toroidally in the direction opposite to the plasma current. The estimated sizes are about a factor of two higher than our results. The difference comes from the different diagnostic technique the estimation was based on.

Maqueda et al reported on the structure of the primary ELM filament structure[17] and the secondary ELM filament structure[16], as well. The radial velocity of the primary filaments were reaching 8 km/s, and the poloidal velocity was estimated to be approximately 11 km/s. The poloidal size of the primary ELM filaments were estimated to be between 40-50mm. Their results based on earlier measurements agree with our findings from a later measurement campaign.

### *2. Comparison with results from MAST*

Measurements of ELM filaments in the SOL on MAST were performed by Kirk et al with Langmuir probes, fast imaging and Thomson-scattering[10].

The fast visible imaging system was able to resolve the spatial structure of the ELM filaments in the SOL for the entire vacuum vessel with the use of wide angle observations. A toroidal mode numbers of 12 is reported from the spatial separation of 75 cm. The NSTX GPI system is covers only a 24 cm × 30 cm (radial × poloidal) plane of the plasma, hence, the complete spatial structure of the ELM filaments cannot be resolved. The filament width was estimated to be between 7.5 cm and 15 cm on MAST. This filament width range is measured with Langmuir-probes and it is significantly larger than the result seen in Fig. 10 (1-6 cm radially, 1-7 cm poloidally). The duration of the ELM crash is reported to be $\approx 100\ \mu$s which is in the same range as our results. The MAST plasma parameters are similar to the NSTX plasma parameters.

| Device | Diagnostic | Measurement | $v_{\mathrm{rad}}$ [km/s] | $v_{\mathrm{pol}}$ [km/s] | $d_{\mathrm{rad}}$ [cm] | $d_{\mathrm{pol}}$ [cm] | $t_{\mathrm{crash}}[\mu\mathrm{s}]$ | Ref. |
|---|---|---|---|---|---|---|---|---|
| NSTX | GPI | $D_\alpha$ | 8 | -11 | - | 4 - 5 | 300 | 16 and 17 |
| (earlier) | Interferometry | $n_{e,int}$ | - | <10 (toroidal) | 10 | - | 400 - 1000 | 27 |
| MAST | Langmuir-probes | $j_{sat}$ | 0.75 | - | 7.5 - 15 | - | 100 | 10 |
| JET | Langmuir-probes | $j_{sat}$ | 1 - 2 | -2 | - | - | 10 - 50 | 12 and 44 |
| ASDEX | HFD | $D_\alpha$ | - | -7.5 - 14 | few cm | few cm | - | 12 |
| | Langmuir-probes | $j_{sat}$ | 0.2-0.8 | - | - | 5-8 | - | 13 |
| | Filament-probe | $j_{sat}$ | 0.5-6 | - | 1-30 | - | - | 45 |
| | FFR | $n_e$ displacement | 3-4 | - | - | - | few $\mu s$ | 46 |
| Alcator C-MOD | 1D GPI | $D_\alpha$ | 1 | - | 0.5 - 1 | - | - | 14 |
| JT60-U | Langmuir-probes | $j_{sat}$ | 0.5-3 | - | 0.5 - 4 | 2 - 6 | 30 | 15 |
| COMPASS | Filament-probe | $j_{sat}$ | 1 | - | - | - | 200 | 47 |
| NSTX | GPI | $D_\alpha$ | 3.3 | -11.4 | 3-7 | 3-7 | 100 | |

TABLE II. Summary of the velocity, size and ELM crash time estimations of the ELM filaments in the SOL from different fusion devices including the diagnostic and the physical quantity measured. The positive sign in the radial velocity denotes the outwards direction. The negative sign in the poloidal velocities denotes the ion diamagnetic direction.

Results of the Langmuir-probe measurements at 3 cm outside the separatrix on MAST show radial propagation velocities of 750 m/s. This value is significantly lower, than the one in Fig. 9. One reason for this difference may be that the probe is only measuring in the scrape-off layer, and can only resolve an average velocity of the filament. According to our observations, the filament reaches its peak radial velocity at the separatrix. The probe measurements on MAST are not performed in that region.

Section V C discusses the underlying theoretical mechanisms behind the dynamics of the ELM filaments. One of these is the current-filament interaction model, hence, the results regarding the ELM filament current is discussed here. In MAST measured magnetic fluctuations for an ELM filament combined with modeling suggest an ELM parallel current of 190 A[48]. It was also pointed out that this value is similar to the edge current density multiplied by the area of the filament.

### 3. Comparison with results from JET

The fine structure of ELMs in the SOL on JET (and ASDEX) was reported by Endler et al[12]. For the analysis on JET, a reciprocating Langmuir-probe system was providing measurements of the ion-saturation current. Measurements in JET showed radial velocities of 1-2 km/s which agreed with the $E \times B$ velocity resulting from an estimation of the plasma and ELM filament parameters. This velocity is significantly lower than the peak velocity at NSTX seen in Fig. 9. In NSTX there was no electric field measurement fast enough to resolve the electric field during the ELM, thus, our results cannot be cross-checked with the corresponding $E \times B$ velocities.

Further investigation by Silva et al provided a more thorough analysis of the radial velocities and mode numbers on JET[44]. Poloidal velocities of 2 km/s are reported for Type-I ELMs, which is significantly lower than the result seen in Fig. 9 (c). The difference might be explained by considering that the pure poloidal velocity is reported on JET, while the GPI measurement can only resolve the apparent poloidal velocity, which may be due in part to the toroidal rotation. The radial velocity found in the JET measurements reached 6 km/s, which agrees with the results in Fig. 9 (a).

In JET, ELM filament currents in the range of $200 - 500$ A were measured, with a most probable current in the order of 400 A[49].

### 4. Comparison with results from ASDEX

The spatial fine structure (on the scale of a few millimeters) of ELMs in the SOL was reported for ASDEX by Endler et al[12]. These results were based on measurements of the $H_\alpha/D_\alpha$ fluctuation diagnostic (HFD) which provided a 16 channel Balmer-alpha light measurement in the SOL. The reported poloidal velocity was between $+14$ km/s and $-7.5$ km/s (the negative sign denotes the ion-diamagnetic direction). This velocity range is comparable to the range of our results in Fig. 9 (c). However, it has to be noted that velocity measurements with a 1D diagnostic can only resolve the velocity components in the direction of the array, which could be distorted by the radial velocity components.

The radial velocities and sizes of ELM filaments on ASDEX were also investigated by Kirk et al[13]. Langmuir probe measurements showed the poloidal extent of the structures were in the $5 - 8$ cm range, which is consistent with our result. However, the measured radial velocities were between $200 - 800$ m/s, which are significantly lower, than our measured peak velocity. One explanation for this could be that the radial velocity in ASDEX was not estimated at the separatrix.

A specially built "filamentary probe" was also utilized on ASDEX to investigate the ELM filaments[45]. The probe measured ion saturation currents with 9 probe tips which are displaced radially, vertically and toroidally, as well. The radial velocity of the ELM filament was reported to be between 0.5 km/s and 6 km/s, and radial sizes of 1 cm to 30 cm were reported. Based on their results they infer that the ELM filaments were generated close to the separatrix. These results agree qualitatively with our results at NSTX, however, their reported radial size of 30 cm exceeds four times our observations. The radial extent of the ELM filament in ASDEX is suspected to depend on the distance between the separatrix and the limiter. In NSTX the usual distance between the separatrix and the RF antenna limiter is $10-15$ cm, and much less for radio-frequency heated shots. This difference could explain the discrepancy of the ELM filament sizes between ASDEX and NSTX.

ELM filaments on ASDEX were also investigated with a fixed frequency reflectometry (FFR)[46]. This diagnostic provided measurements of the radial displacement of a density layer, which can be used to estimate the radial propagation velocity of the ELM filaments. The reported radial velocity was about $3-4$ km/s. The duration of the crash was estimated to be only a few microseconds. The poloidal size of the ELM filaments was estimated to be in the range of $5.75-11.5$ cm. The magnitude of this estimated velocity agrees with our results seen in Fig. 9. The duration of the crash, however, is about 10 times smaller than at NSTX, which is is the range of $\approx 100\mu$s. The reason for this discrepancy may be the diagnostic method itself. The reflectometry measures the reflected wave from a certain fixed density area. The density of the ELM filament is changing rapidly during its motion, hence, the peak is only seen for a short amount of time.

In AUG, measurements showed that ELM filaments carried a substantial field aligned current, estimated to be on the order of 2 kA with large uncertainty[50].

#### *5. Comparison with results from other machines*

ELM filaments were investigated on many other machines, as well.

Terry et al performed ELM filament measurements with a 1D gas-puff imaging array on Alcator C-MOD[14]. The median radial velocity of the ELM filaments was reported to be 1 km/s with spikes up to 8 km/s. The radial size of the ELM filament was reported to be between $0.5-1$ cm. The magnitude of the radial velocity agrees with our results qualitatively. The size of the ELM filament was significantly lower than at NSTX.

Asakura et al investigated the high field side and low field side ELM filaments on JT-60U[15] with Langmuir probes. The radial propagation velocities of the LFS filaments were estimated to be between 0.5 km/s and 3 km/s. The radial size of the ELM filament is found to be in between 0.5 cm and 4 cm, while the poloidal size to be $2-6$ cm. These results agree with our results on NSTX seen in Fig. 9 (a) and Fig. 10 (a) and (c).

Spolaore et al measured the ELM filaments in the scrape-off layer of the COMPASS tokamak with a "filament probe"[47]. The radial velocity was estimated to be 1 km/s in the far SOL and the typical ELM crash lasted for approximately 200 $\mu$s.

As one can see from these comparisons and in Table II, quantitative agreement is found between the results on other machines and our results from NSTX. The discrepancies could have been due to the limitations of the diagnostics in most cases.

## VI. SUMMARY

Edge localized modes (ELMs) are quasi-periodic events at the plasma edge causing significant particle and energy losses from the plasma. The dynamics of the most violent part of the ELM cycle, the ELM crash, were investigated utilizing the gas-puff imaging (GPI) diagnostic on NSTX. This diagnostic enabled the characterization of the ELM crash and its associated ELM filaments. An ELM database was built from 2010 H-mode plasma discharges using high signal-to-noise ratio GPI measurements.

A frame-by-frame velocity estimation method was developed in order to characterize the propagation of the filaments during an ELM event. A frame-by-frame structure identification and fitting method was developed to characterize their sizes, and also their velocities. These methods were tested and validated, and found to provide an accurate estimate of the ELM filament properties.

During a preliminary analysis, typical ELM filaments were found to propagate radially outwards and poloidally in the ion-diamagnetic direction. No significant size change was found compared to the regular filaments (blobs) of the background turbulence. The number of structures present during the ELM crash was found to be lower than during the background turbulence.

The analysis methods were automated and applied to all 159 ELM events in the database. In order to characterize the behavior of the ELM crash, the distribution functions of the parameters and their median and 10th and 90th percentile values were calculated around the ELM crash times. The following experimental results were found during the analysis corresponding to the propagation velocity and the structure sizes.

- The characterizing radial velocity of the ELM filament peaked at 3.3 km/s outwards. Its median poloidal velocity peaked at 11.4 km/s in the ion diamagnetic direction at the crash. The ELM crashes have a characterizing time of approximately 100 $\mu$s.
- The characterizing radial and poloidal sizes of the ELM filaments were 49 mm and 47 mm, respectively. The median radial and poloidal sizes are close to each other at the ELM crash: the ELM filament has a nearly circular characterizing shape.
- During the characterizing behavior of the ELM filament, it was born close to the separatrix, and then it propagated from $\mathrm{r}-\mathrm{r}_{\mathrm{sep}}=20$ mm to $\mathrm{r}-\mathrm{r}_{\mathrm{sep}}=67$ mm. The propagation of the ELM filament set on $\mathrm{t}=25$ $\mu$s before reaching its peak radial velocity.

These results were found to be consistent with experimental results from other fusion devices, at least within the experimental limitations. The following novel results were found during the analysis, which have not been seen before on other machines.

- The median number of structures is $\mathrm{N}=1$ at the ELM crash meaning that the filaments coalesce into a single structure, the ELM filament, within the GPI field of view.

- The characterizing radial velocity of the ELM filament is increasing close to linearly with the filament's distance from the separatrix.
- There is positive correlation between the radial and poloidal sizes of the filaments before and after the ELM.

Two theoretical models were identified which could explain certain aspects of our observations: the curvature-interchange mechanism and the current-filament interaction model. The radial acceleration of the ELM filaments measured by GPI were compared with these originating from the two analytical theories. The conclusion of the comparison was that either mechanism could have sufficient strength to contribute to the radial acceleration of the ELM filament. However, the poloidal acceleration and the coalescence of the ELM filaments cannot be explained with the curvature drive mechanism alone. The current-filament interaction model could much better account for both of these aspects of the observations.

One of the most striking findings in this paper, however, cannot be explained by these theories. The characterizing radial velocity of the ELM filament increases linearly with the distance of the filament from the separatrix. A definitive explanation cannot be given to why the ELM filaments behave in such a way based on the theoretical physical mechanisms.

Looking ahead to future devices, unmitigated ELMs would cause cyclical and unacceptably high heat loads to plasma-facing surfaces, while mitigated ELMs would nevertheless enhance erosion of main chamber walls. Understanding the underlying mechanisms behind ELM structure, motion, lifetime and energy deposition in the SOL remains critically important. The time history of the ELM determines in part the energy deposition rate on the divertor while the motion and size of the ELM filament determines the location and cross-sectional area where that deposition occurs. It is intended that the present mid-plane ELM observations will contribute to the full characterization of the three-dimensional structure and motion of the filaments, towards development of models that can predict their impact on plasma-material interactions.

## ACKNOWLEDGMENTS

The authors would like to thank R.J. Maqueda for collaboration on the NSTX GPI diagnostic, B. LeBlanc for the Thomson scattering data, S. Sabbagh for the EFIT results, S. Kaye and R. Maingi for their helpful suggestions on the paper, and the NSTX/NSTX-Upgrade Team for their support for this work. The corresponding author would like to thank T. Looby and S. Zoletnik for the fruitful discussions. This work was supported by U.S. DOE Contract No. DE-AC02-09CH11466 (PPPL) and Office of Fusion Energy Sciences, under Award Number DE-FG02-97ER54392.

## DATA AVAILABILITY

The data that support the findings of this study are openly available at http://arks.princeton.edu/ark:/88435/dsp011v53k104h reference number 29.

[1] F. Wagner, "A quarter-century of H-mode studies," Plasma Physics and Controlled Fusion **49**, B1–B33 (2007).

[2] A. W. Leonard, "Edge-localized-modes in tokamaks," Physics of Plasmas **21**, 090501 (2014), https://doi.org/10.1063/1.4894742.

[3] A. Loarte, G. Saibene, R. Sartori, D. Campbell, M. Becoulet, L. Horton, T. Eich, A. Herrmann, G. Matthews, N. Asakura, A. Chankin, A. Leonard, G. Porter, G. Federici, G. Janeschitz, M. Shimada, and M. Sugihara, "Characteristics of type i ELM energy and particle losses in existing devices and their extrapolation to ITER," Plasma Physics and Controlled Fusion **45**, 1549–1569 (2003).

[4] T. Eich, B. Sieglin, A. Thornton, M. Faitsch, A. Kirk, A. Herrmann, and W. Suttrop, "ELM divertor peak energy fluence scaling to ITER with data from JET, MAST and ASDEX upgrade," Nuclear Materials and Energy **12**, 84 – 90 (2017), proceedings of the 22nd International Conference on Plasma Surface Interactions 2016, 22nd PSI.

[5] J. W. Connor, "A review of models for ELMs," Plasma Physics and Controlled Fusion **40**, 191–213 (1998).

[6] P. Snyder, H. Wilson, J. Ferron, L. Lao, A. Leonard, D. Mossessian, M. Murakami, T. Osborne, A. Turnbull, and X. Xu, "ELMs and constraints on the H-mode pedestal: peeling–ballooning stability calculation and comparison with experiment," Nuclear Fusion **44**, 320–328 (2004).

[7] A. Kirk, D. Dunai, M. Dunne, G. Huijsmans, S. Pamela, M. Becoulet, J. Harrison, J. Hillesheim, C. Roach, and S. Saarelma, "Recent progress in understanding the processes underlying the triggering of and energy loss associated with type I ELMs," Nuclear Fusion **54**, 114012 (2014).

[8] H. Zohm, "Edge localized modes (ELMs)," Plasma Physics and Controlled Fusion **38**, 105–128 (1996).

[9] N. Nishino, L. Roquemore, R. Kaita, S. J. Zweben, D. Johnson, H. W. Kugel, R. Maqueda, C. Bush, R. Maingi, V. Soukhanovskii, F. Paolaetti, S. A. Sabbagh, and N. team, "First results with the nstx fast divertor camera," Journal of Plasma and Fusion Research **78**, 1278–1279 (2002).

[10] A. Kirk, H. R. Wilson, G. F. Counsell, R. Akers, E. Arends, S. C. Cowley, J. Dowling, B. Lloyd, M. Price, and M. Walsh (MAST Team), "Spatial and temporal structure of edge-localized modes," Phys. Rev. Lett. **92**, 245002 (2004).

[11] H. R. Wilson and S. C. Cowley, "Theory for explosive ideal magnetohydrodynamic instabilities in plasmas," Phys. Rev. Lett. **92**, 175006 (2004).

[12] M. Endler, I. García-Cortés, C. Hidalgo, G. F. Matthews, A. Team, and J. Team, "The fine structure of ELMs in the scrape-off layer," Plasma Physics and Controlled Fusion **47**, 219–240 (2005).

[13] A. Kirk, T. Eich, A. Herrmann, H. W. Muller, L. D. Horton, G. F. Counsell, M. Price, V. Rohde, V. Bobkov, B. Kurzan, J. Neuhauser, H. Wilson, the ASDEX Upgrade, and M. Teams, "The spatial structure of type-I ELMs at the mid-plane in ASDEX upgrade and a comparison with data from MAST," Plasma Physics and Controlled Fusion **47**, 995–1013 (2005).

[14] J. L. Terry, I. Cziegler, A. E. Hubbard, J. A. Snipes, J. W. Hughes, M. J. Greenwald, B. LaBombard, Y. Lin, P. Phillips, and S. Wukitch, "The dynamics and structure of edge-localized-modes in Alcator C-Mod," Journal of Nuclear Materials **363-365** (2007), 10.1016/j.jnucmat.2007.01.266.

[15] N. Asakura, H. Kawashima, N. Ohno, G. Matsunaga, T. Nakano, and N. Oyama, "ELM propagation in the low- and high-field-side scrape-off layer of the JT-60U tokamak," Journal of Physics: Conference Series **123**, 012009 (2008).

[16] R. Maqueda, R. Maingi, and J.-W. Ahn, "Secondary ELM filaments in NSTX," Journal of Nuclear Materials **390-391**, 843 – 846 (2009), proceedings of the 18th International Conference on Plasma-Surface Interactions in Controlled Fusion Device.

[17] R. Maqueda and R. Maingi, "Primary edge localized mode filament structure in the national spherical torus experiment," Physics of Plasmas **16**, 056117 (2009), https://doi.org/10.1063/1.3085798.

[18] G. S. Yun, W. Lee, M. J. Choi, J. Lee, H. K. Park, B. Tobias, C. W. Domier, N. C. Luhmann, A. J. H. Donné, and J. H. Lee (KSTAR Team), "Two-

dimensional visualization of growth and burst of the edge-localized filaments in KSTAR H-Mode plasmas," Phys. Rev. Lett. **107**, 045004 (2011).

[19] J. Adamek, D. Tskhakaya, A. Devitre, J. Cavalier, J. Horacek, M. Komm, M. Sos, P. Bilkova, P. Böhm, J. Seidl, V. Weinzettl, P. Vondracek, T. Markovic, M. Hron, R. Panek, and and, "On the transport of edge localized mode filaments in the tokamak scrape-off layer," Nuclear Fusion **60**, 096014 (2020).

[20] C. Ham, A. Kirk, S. Pamela, and H. Wilson, "Filamentary plasma eruptions and their control on the route to fusion energy," Nature Reviews Physics **2**, 159–167 (2020).

[21] S. J. Zweben, J. L. Terry, D. P. Stotler, and R. J. Maqueda, "Invited review article: Gas puff imaging diagnostics of edge plasma turbulence in magnetic fusion devices," Review of Scientific Instruments **88**, 041101 (2017), https://doi.org/10.1063/1.4981873.

[22] S. Zweben, R. Maqueda, D. Stotler, A. Keesee, J. Boedo, C. Bush, S. Kaye, B. LeBlanc, J. Lowrance, V. Mastrocola, R. Maingi, N. Nishino, G. Renda, D. Swain, J. Wilgen, and the NSTX Team, "High-speed imaging of edge turbulence in NSTX," Nuclear Fusion **44**, 134–153 (2003).

[23] S. J. Zweben, D. P. Stotler, F. Scotti, and J. R. Myra, "Two-dimensional turbulence cross-correlation functions in the edge of NSTX," Physics of Plasmas **24**, 102509 (2017), https://doi.org/10.1063/1.5002695.

[24] M. Ono, S. Kaye, Y.-K. Peng, G. Barnes, W. Blanchard, M. Carter, J. Chrzanowski, L. Dudek, R. Ewig, D. Gates, R. Hatcher, T. Jarboe, S. Jardin, D. Johnson, R. Kaita, M. Kalish, C. Kessel, H. Kugel, R. Maingi, R. Majeski, J. Manickam, B. McCormack, J. Menard, D. Mueller, B. Nelson, B. Nelson, C. Neumeyer, G. Oliaro, F. Paoletti, R. Parsells, E. Perry, N. Pomphrey, S. Ramakrishnan, R. Raman, G. Rewoldt, J. Robinson, A. Roquemore, P. Ryan, S. Sabbagh, D. Swain, E. Synakowski, M. Viola, M. Williams, J. Wilson, and N. Team, "Exploration of spherical torus physics in the NSTX device," Nuclear Fusion **40**, 557–561 (2000).

[25] Y. Sechrest, T. Munsat, D. Battaglia, and S. Zweben, "Two-dimensional characterization of ELM precursors in NSTX," Nuclear Fusion **52**, 123009 (2012).

[26] B. P. LeBlanc, R. E. Bell, D. W. Johnson, D. E. Hoffman, D. C. Long, and R. W. Palladino, "Operation of the NSTX Thomson scattering system," Review of Scientific Instruments **74**, 1659–1662 (2003), https://doi.org/10.1063/1.1532763.

[27] R. Maingi, M. G. Bell, E. D. Fredrickson, K. C. Lee, R. J. Maqueda, P. Snyder, K. Tritz, S. J. Zweben, R. E. Bell, T. M. Biewer, C. E. Bush, J. Boedo, N. H. Brooks, L. Delgado-Aparicio, C. W. Domier, D. A. Gates, D. W. Johnson, R. Kaita, S. M. Kaye, H. W. Kugel, B. P. LeBlanc, N. C. Luhmann, J. E. Menard, D. Mueller, H. Park, R. Raman, A. L. Roquemore, S. A. Sabbagh, V. A. Soukhanovskii, T. Stevenson, and D. Stutman, "Characterization of small, Type V edge-localized modes in the national spherical torus experiment," Physics of Plasmas **13**, 092510 (2006), https://doi.org/10.1063/1.2226986.

[28] M. Lampert, "NSTX GPI ELM database," https://github.com/fusion-flap/flap_nstx/blob/master/db/ELM_findings_mlampert_velocity_good.csv (2020).

[29] M. Lampert, A. Diallo, J. Myra, and S. Zweben, "Dynamics of filaments during the edge-localized mode crash on NSTX," http://arks.princeton.edu/ark:/88435/dsp011v53k104h (2021).

[30] J. D. Hunter, "Matplotlib: A 2d graphics environment," Computing in Science & Engineering **9**, 90–95 (2007).

[31] C. J. Ham, S. C. Cowley, G. Brochard, and H. R. Wilson, "Nonlinear stability and saturation of ballooning modes in tokamaks," Phys. Rev. Lett. **116**, 235001 (2016).

[32] C. J. Ham, S. C. Cowley, G. Brochard, and H. R. Wilson, "Nonlinear ballooning modes in tokamaks: stability and saturation," Plasma Physics and Controlled Fusion **60**, 075017 (2018).

[33] A. Kirk, G. F. Counsell, G. Cunningham, J. Dowling, M. Dunstan, H. Meyer, M. Price, S. Saarelma, R. Scannell, M. Walsh, H. R. Wilson, and the MAST team, "Evolution of the pedestal on MAST and the implications for ELM power loadings," Plasma Physics and Controlled Fusion **49**, 1259–1275 (2007).

[34] T. Evans, J. Yu, M. Jakubowski, O. Schmitz, J. Watkins, and R. Moyer, "A conceptual model of the magnetic topology and nonlinear dynamics of elms," Journal of Nuclear Materials **390-391**, 789 – 792 (2009), proceedings of the 18th International Conference on Plasma-Surface Interactions in Controlled Fusion Device.

[35] J. R. Myra, "Current carrying blob filaments and edge-localized-mode dynamics," Physics of Plasmas **14**, 102314 (2007), https://doi.org/10.1063/1.2776900.

[36] D. A. D'Ippolito, J. R. Myra, and S. J. Zweben, "Convective transport by intermittent blob-filaments: Comparison of theory and experiment," Physics of Plasmas **18**, 060501 (2011), https://doi.org/10.1063/1.3594609.

[37] S. Krasheninnikov, D. Ryutov, and Y. Guanghui, "Large plasma pressure perturbations and radial convective transport in a tokamak," Journal of Plasma and Fusion Research SERIES **6**, 139–143 (2004).

[38] S. I. Krasheninnikov, D. A. D'Ippolito, and J. R. Myra, "Recent theoretical progress in understanding coherent structures in edge and sol turbulence," Journal of Plasma Physics **74**, 679–717 (2008).

[39] M. W. Bongard, R. J. Fonck, C. C. Hegna, A. J. Redd, and D. J. Schlossberg, "Measurement of peeling mode edge current profile dynamics," Phys. Rev. Lett. **107**, 035003 (2011).

[40] M. Bongard, K. Thome, J. Barr, M. Burke, R. Fonck, E. Hinson, A. Redd, and D. Schlossberg, "Characterization of peeling modes in a low aspect ratio tokamak," Nuclear Fusion **54**, 114008 (2014).

[41] W. Fundamenski, V. Naulin, T. Neukirch, O. E. Garcia, and J. J. Rasmussen, "On the relationship between ELM filaments and solar flares," Plasma Physics and Controlled Fusion **49**, R43–R86 (2007).

[42] K. Bodi, S. I. Krasheninnikov, and A. I. Smolyakov, "Blob dynamics in an inhomogeneous plasma," Physics of Plasmas **15**, 102304 (2008), https://doi.org/10.1063/1.2993211.

[43] H. R. Wilson and S. C. Cowley, "Theory for explosive ideal magnetohydrodynamic instabilities in plasmas," Phys. Rev. Lett. **92**, 175006 (2004).

[44] C. Silva, W. Fundamenski, A. Alonso, B. Gonçalves, C. Hidalgo, M. A. Pedrosa, R. A. Pitts, and M. S. and, "Reciprocating probe measurements of ELM filaments on JET," Plasma Physics and Controlled Fusion **51**, 105001 (2009).

[45] A. Schmid, A. Herrmann, and H. W. M. and, "Experimental observation of the radial propagation of ELM induced filaments on ASDEX upgrade," Plasma Physics and Controlled Fusion **50**, 045007 (2008).

[46] J. Vicente, G. D. Conway, M. E. Manso, H. W. Müller, C. Silva, F. da Silva, L. Guimarãis, and A. Silva, "H-mode filament studies with reflectometry in ASDEX upgrade," Plasma Physics and Controlled Fusion **56**, 125019 (2014).

[47] M. Spolaore, K. Kovařík, J. Stöckel, J. Adamek, R. Dejarnac, I. Ďuran, M. Komm, T. Markovic, E. Martines, R. Panek, J. Seidl, and N. Vianello, "Electromagnetic ELM and inter-ELM filaments detected in the COMPASS Scrape-Off Layer," Nuclear Materials and Energy **12**, 844 – 851 (2017), proceedings of the 22nd International Conference on Plasma Surface Interactions 2016, 22nd PSI.

[48] A. Kirk, N. B. Ayed, G. Counsell, B. Dudson, T. Eich, A. Herrmann, B. Koch, R. Martin, A. Meakins, S. Saarelma, R. Scannell, S. Tallents, M. Walsh, H. R. Wilson, and the MAST team, "Filament structures at the plasma edge on MAST," Plasma Physics and Controlled Fusion **48**, B433–B441 (2006).

[49] P. Migliucci and V. Naulin, "Magnetic signature of current carrying edge localized modes filaments on the Joint European Torus tokamak," Physics of Plasmas **17**, 072507 (2010), https://doi.org/10.1063/1.3436608.

[50] N. Vianello, V. Naulin, R. Schrittwieser, H. W. Müller, M. Zuin, C. Ionita, J. J. Rasmussen, F. Mehlmann, V. Rohde, R. Cavazzana, and M. Maraschek (ASDEX Upgrade Team), "Direct observation of current in Type-I Edge-Localized-Mode filaments on the ASDEX Upgrade tokamak," Phys. Rev. Lett. **106**, 125002 (2011).

[51] E. W. Weisstein, "Least squares fitting–polynomial," https://mathworld.wolfram.com/LeastSquaresFittingPolynomial.html (2020).

# Appendix

## A1. NORMALIZATION OF THE NEUTRAL GAS RESPONSE

In order to get an accurate estimate of the structure velocities and sizes from the GPI images, normalization of the GPI frames is necessary. The velocity estimation method presented in Section III A is biased towards the spatial displacement of the structure with the highest intensity. In most cases, despite the ELM crash, the most intense structure in the frame is the stationary response of the gas to the background plasma. Normalizing each frame can tackle this problem as described below.

During GPI measurements it is assumed that the measured emission intensity is a function of the local temperature and density and the neutral density of the gas. No independent measurement is available for the neutral density distribution at the location of the GPI neutral gas. However, the timescales of the fluctuations ($\approx 10\ \mu s$) and the neutral density ($\approx 1\ ms$) are several magnitudes apart. One can separate the response of the neutrals to the background plasma from their response to the fluctuations by low-pass temporal filtering the GPI signal. The filtering was performed with 1 kHz cut-off frequency, Elliptic IIR (infinite impulse response) filter kernel and symmetric filtering. Symmetric filtering was necessary in order to remove the phase shifting property of the filter.

This method isolates the rapidly fluctuating part of the GPI signal, which is assumed to be due to the density and temperature perturbations of the ELM filament. Although it is possible that the neutral density in the gas cloud changes due to these perturbations, we assume that neutral density perturbations do not significantly affect the estimates of filament velocity and structure. This is the usual assumption in the experimental interpretation of GPI[21], since there is no way to directly measure the local neutral density fluctuations.

## A2. TWO-DIMENSIONAL SPATIAL TREND SUBTRACTION

A one-dimensional $\mathrm{n_{th}}$ order polynomial fit is readily available in most data analysis environments, however, a two-dimensional polynomial fit had to be developed. A two-dimensional $\mathrm{n_{th}}$ order polynomial can be written as Eqn. A1.

$$f(x,y) = \sum_{i=0}^{n} \sum_{j=0}^{n-i} c_{i,j} x^i y^j \tag{A1}$$

where $\mathrm{f(x,y)}$ is the 2D polynomial, n is the order of the polynomial, $\mathrm{c_{i,j}}$ are the coefficients, and x and y are the coordinates in the two dimensions. This expression realizes a two-dimensional polynomial which can be fit onto each $64 \times 80$ pixel GPI frame by a least square fit method[51] then subtracted from it frame-by-frame.

## A3. FRAME-BY-FRAME TWO-DIMENSIONAL SPATIAL DISPLACEMENT ESTIMATION

During the velocity estimation presented in Sec. III the 2D cross-correlation function is utilized to give an estimate on the velocity. The definition of the 2D spatial CCF function is given by Eqn. A2.

$$CCF_{(f_k,f_{k-1})}(\kappa_x,\kappa_y,t_k) = \frac{COV_{(f_k,f_{k-1})}}{\sqrt{ACF_{(f_k)} \cdot ACF_{(f_{k-1})}}} \tag{A2}$$

where $\mathrm{COV_{(f_k,f_{k-1})}}$ is the spatial co-variance between frame $\mathrm{f_k}$ at time $\mathrm{t_k}$ and frame $\mathrm{f_{k-1}}$ at time $\mathrm{t_{k-1}}$ given by Eqn. A3. $\mathrm{ACF_{(f_k)}}$ is the spatial auto-correlation function of frame $\mathrm{f_k}$ given by Eqn. A4.

$$\begin{aligned} COV_{(f_k,f_{k-1})}(\kappa_x,\kappa_y,t_k) &= \\ C_{\kappa_x,\kappa_y} \cdot \sum_{i,j} f(x_i-\kappa_x, y_j-\kappa_y, t_k) \cdot f(x_i,y_j,t_{k-1}) \end{aligned} \tag{A3}$$

$$\begin{aligned} ACF_{(f_k)}(\kappa_x,\kappa_y,t_k) &= \\ C_{\kappa_x,\kappa_y} \cdot \sum_{i,j} f(x_i-\kappa_x, y_j-\kappa_y, t_k) \cdot f(x_i,y_j,t_k) \end{aligned} \tag{A4}$$

where i and j are indexing the x and y pixel coordinates, $\kappa_\mathrm{x}$ and $\kappa_\mathrm{y}$ are the spatial displacements, and $\mathrm{C}_{\kappa_\mathrm{x},\kappa_\mathrm{y}} = (\mathrm{n_x} - \kappa_\mathrm{x}) \cdot (\mathrm{n_y} - \kappa_\mathrm{y})$ is a normalization factor, which equals to the overlapping number of pixels. The summation is done for overlapping pixels only.

## A4. THE STRUCTURE FINDING ALGORITHM

The steps of the algorithm were the following:

1. Plot the frame as a contour plot with a pre-defined number of contour levels.
2. Find the closed path(s) with the highest intensity.
3. This defines the first, initial structure(s).
4. Find the closed path(s) with the second highest intensity.
5. Check if the path of this level contains (encloses) one of the paths in the previous level.
6. If yes: belongs to the same structure.
7. If not: create a new structure.
8. Repeat from step 4 until the algorithm runs out of levels.
9. Delete the structures with a number of paths below a defined number.

At the end of the calculation, falsely identified structures could exist due to noise in the GPI measurement. In order to mitigate this caveat, a threshold was established based on the number of paths a structure must contain. This threshold was set to 5 (roughly 10% of all the contour levels). In the last step, the structures which do not reach this threshold are removed.

## A5. VALIDATION OF THE VELOCITY AND STRUCTURE SIZE ESTIMATION

Before applying the methods of Sec. III to determine the structural dynamics of the filaments associated with ELMs, the velocity estimation and structure finding algorithm were validated against a synthetic GPI signal.

Here we are presenting a worst-case scenario testing of the 2D cross-correlation based velocity estimation method and the structure finding mechanism. During the testing the simulated filament is propagating in the frame in a way, where at the edge of the frame, it is present with its full intensity, and another filament is already present at the top of the frame. During the real GPI measurements of ELM filaments this rarely occurs and the algorithms give a more accurate result.

The spatial geometry of the synthetic input signal was exactly the same as the NSTX GPI with 64 × 80 pixels. The synthetic input signal was generated for 1 ms with 400 frames as it would have been in the real measurement. A stationary background was added to the image to simulate the response of the GPI gas neutrals to the background plasma. Eqn. A5 simulated the filaments seen in the actual GPI measurement.

$$
\begin{aligned}
I(R,z,t) &= \frac{A\sin(\phi)f(\phi,FF)}{\sqrt{2\pi\sigma}}\cdot e^{\frac{1}{2}\left(\frac{R-(R_0+v_{rad}\cdot t)}{\sigma}\right)^2} \\
\phi &= \frac{\pi}{d_{pol}}(z-(z_0+v_{pol}\cdot t))+\phi_0
\end{aligned}
\qquad \text{(A5)}
$$

where A is the amplitude, $\sigma = d_{rad}/2.355$, where $d_{rad}$ is the radial size, $R_0$ is the initial radial position of the input structure, $v_{rad}$ is the radial velocity, $d_{pol}$ is the poloidal size, $z_0$ is the initial vertical position, $v_{pol}$ is the poloidal velocity $\phi_0$ is the initial phase. Function "f" is a special square wave function with a fill factor of FF. This filters the signal in a way where only the $n^{th}$ positive half period of the sine wave remains. This realizes a periodically occurring filament which propagates in the poloidal and radial direction. Its poloidal intensity profile is sinusoidal, and its radial profile is Gaussian.

Figure 15 depicts the results of the testing of the cross-correlation based velocity estimation and the structure parameter estimation methods on the aforementioned synthetic signal. Figures 15 (a) and (b) show two input frames of the normalized synthetic GPI signal along with the synthetic structures depicted with an orange ellipse in each frame. The structure in the synthetic signal was set to have $v_{rad} = 0$ and $v_{pol} = 3$ km/s radial and poloidal velocities, respectively. The radial and poloidal sizes were both set to $d_{rad} = d_{pol} = 50$ mm. No further effects were added to the structure, thus, its shape was not changing during the synthetic signal generation, only its center position was modified.

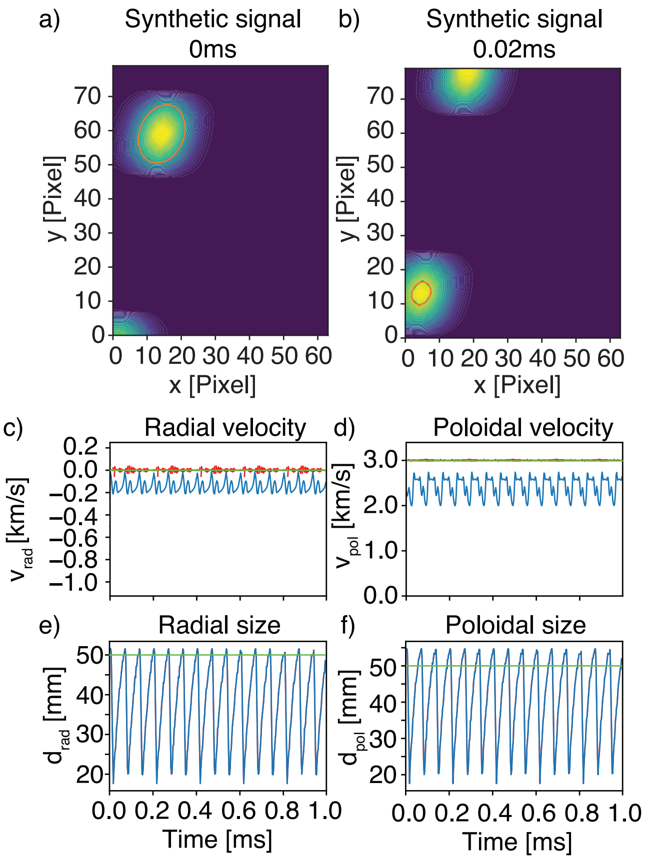

FIG. 15. Input of the synthetic signal a) Synthetic GPI signal at 0 ms with one found structure; b) Synthetic signal 20 $\mu$s after a), after the structure in a) has partially left the measurement range. The structure found is smaller than the input due to its partial presence in the frame; c) Estimated radial velocity from the CCF method (blue) and from the structure centers (red), where the green line depicts the input setting; d) Estimated poloidal velocity (same notation as for c); e) Estimated radial structure size from the structure fitting (the green line depicts the setting); f) Estimated poloidal structure size (the green line depicts the setting).

One can see that just like in the ELM crash case in Fig. 7, the structures just entering the frame or already exiting, are not found. Furthermore, Fig. 15 (a) shows that the structure size is accurately estimated for the frame where the structure is entirely within the measurement frame. However, in Fig. 15 (b) one can see, that the structure is only partially inside the frame, thus, its size is underestimated. This shows one of the limitations of the structure finding algorithm combined with the GPI measurement.

Fig. 15 (c) and (d) show the estimated radial and poloidal velocities, respectively, estimated by the cross-correlation based method in blue. The red plot in both figures shows the velocity estimate calculated from the displacement of the fit ellipse's center. One can see that the cross-correlation based velocity estimation method estimates an average of -150 m/s radial velocity instead of the input 0 m/s velocity, while the estimate from the center of the structure is more accurate, with an average of approximately 0 m/s. In the case of the poloidal velocity estimation, the average estimated velocity is 2.4 km/s which is below the set 3 km/s.

Fig. 15 (e) and (f) depict the estimates for the radial and poloidal sizes, respectively. As one can see, the average estimated radial and poloidal sizes are both approximately 35mm. This effect is a result of the partially framed structures of which sizes are consistently underestimated when they are not entirely in the frame of the measurement. When they are in the frame entirely, the estimated size becomes more accurate.